1978

Calculation of supersonic viscous flow over delta wings with sharp subsonic leading edges

Yvon Clovis Vigneron
Iowa State University

Calculation of supersonic viscous flow over delta wings with sharp subsonic leading edges

by

Yvon Clovis Vigneron

A Dissertation Submitted to the
Graduate Faculty in Partial Fulfillment of
The Requirements for the Degree of
DOCTOR OF PHILOSOPHY
Major: Aerospace Engineering

Approved:

Signature was redacted for privacy.

In Charge of Major Work

Signature was redacted for privacy.

For the Major Department

Signature was redacted for privacy.

For the Graduate College

Iowa State University
Ames, Iowa

1978

TABLE OF CONTENTS

	Page
INTRODUCTION	1
FIRST METHOD: CONICAL APPROXIMATION	5
Governing Equations	5
Grid Generation	8
Numerical Solution of Equations	10
Numerical algorithm	10
Boundary conditions	11
Initial conditions	12
SECOND METHOD: PARABOLIC APPROXIMATION	13
Governing Equations	13
Importance of the Streamwise Pressure Gradient	15
Previous analysis	15
Present analysis	16
Linear stability analysis	20
Numerical Solution of Equations	31
Numerical algorithm	31
Boundary conditions	34
Initial conditions	35
RESULTS AND DISCUSSION	36
Test Conditions	36
Results from the Conical Approximation	36
Test case No. 1	36
Test case No. 2	38
Test case No. 3	49

Results for the Parabolic Approximation 49

Test case No. 1 52

Test case No. 2 56

Computation Times 59

CONCLUSIONS 60

REFERENCES 61

ACKNOWLEDGMENTS 64

APPENDIX A: GOVERNING EQUATIONS 65

APPENDIX B: "SHOCK-FITTING" PROCEDURES 68

Conical Approximation 68

Parabolic Approximation 70

APPENDIX C: JACOBIANS $\partial F_2/\partial U_2$, $\partial G_2/\partial U_2$, and $\partial E_2^*/\partial U_2$ 72

INTRODUCTION

The prediction of three-dimensional viscous flows with large separated regions is an essential part of aircraft aerodynamics. For wings with highly swept leading edges the flow on the suction side tends to spiral in the manner of a vortex parallel to the leading edge. The presence of the rotating flow provides lift augmentation at low supersonic speeds, up to the point where the flow breaks down due to viscous effects. Unfortunately, such viscous, vortex flows do not allow easy analysis. A classical example, which illustrates the nature and difficulties of these flows, is the delta wing problem.

The supersonic flow around a delta wing at angle of attack with sharp subsonic leading edges is shown schematically in Figure 1. A conical shock originating from the apex envelops the wing. A free shear layer separates from the leading edges and rolls up into a pair of conically growing vortices. As the angle of attack increases, the reattachment lines of these main vortices on the upper surface move inboard, and secondary vortices appear under the main ones, with opposite circulation.

Previous analytical studies to solve this flow field (see Reference 1) have used the leading edge suction analogy (2), linear slender wing theory (3), or detached flow methods (4). These studies are all fundamentally inviscid. Some of them assume a model with two concentrated vortices lying on top of the wing and make use of a Kutta condition which requires the flow to separate tangentially from the leading edges. Thus, the viscous nature of the flow is contained in these conditions. Unfortunately, all these methods only give approximate results. A recent approach (5) uses a

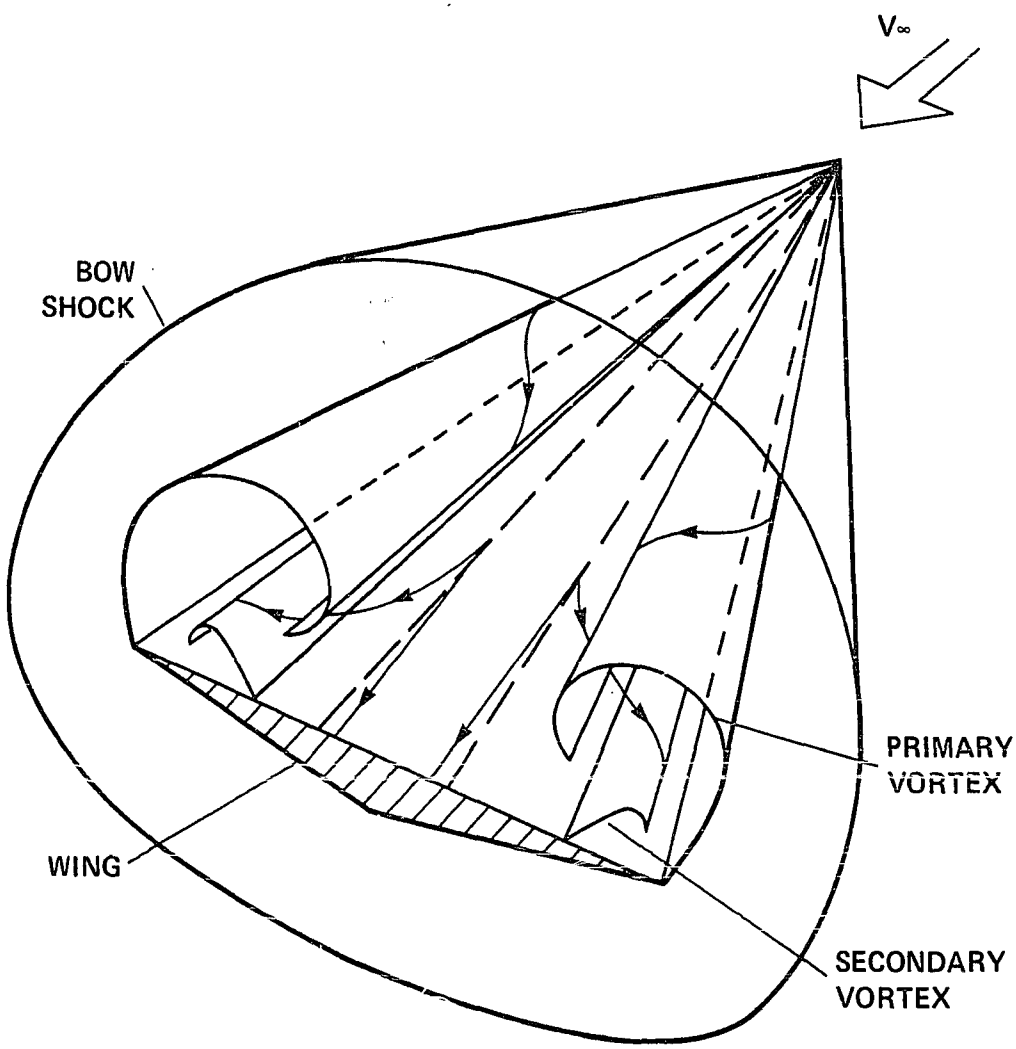

Figure 1. General features of the flow

potential flow technique along with modeling of the main vortex sheet. However, it does not take into account secondary separation and does not apply as yet to supersonic flow. Finite-difference inviscid calculations (6) have also been performed but they do not account for the large viscous effects on the leeward side of the wing.

In the present investigation, two complementary procedures are developed which avoid the shortcomings of the above methods by solving the complete viscous and inviscid flow field about delta wings. Moreover, solutions are obtained without the costly computing requirements of a fully three-dimensional, time-dependent, finite-difference technique.

In the first approach, the flow is assumed to be conically self-similar. This approximation is suggested by the results of experiments for supersonic flows around conical bodies and wings (7,8). The resulting Navier-Stokes equations are solved at a given Reynolds number with a time-marching explicit finite-difference algorithm. A similar idea has already been used for cones at angles of attack (9) and is currently applied to delta wings with supersonic leading edges (10). These calculations capture the bow shock, however, and are limited by a rather restrictive geometry. The present method treats the shock as a sharp discontinuity and allows for a completely general cross-sectional shape and distribution of the finite-difference grid points.

In the second approach, only the streamwise viscous derivatives are neglected in the steady Navier-Stokes equations. This has been called the "parabolic" approximation because the equations take on the parabolic mathematical form with respect to the streamwise direction (11). The solution is marched downstream from a given initial station. Previous

investigators have used this approach, along with an implicit, iterative finite-difference scheme, to compute the supersonic flow over circular cones at angle of attack (12,13). This paper presents a new implicit, non-iterative algorithm which provides better computational efficiency than the published techniques and is not restricted to conical shapes.

In the following pages, a detailed description of these two procedures is given. Some laminar results for cones and delta wings are shown and comparisons are made with existing computations and available experimental data.

FIRST METHOD: CONICAL APPROXIMATION

Governing Equations

The governing equations for an unsteady three-dimensional flow without body forces or external heat addition can be written in nondimensional strong conservation-law form in Cartesian coordinates as:

$$\frac{\partial U}{\partial t} + \frac{\partial (E - E_v)}{\partial x} + \frac{\partial (F - F_v)}{\partial y} + \frac{\partial (G - G_v)}{\partial z} = 0 \tag{1}$$

where E, F, G are functions of U and E_v, F_v, G_v are functions of U, U_x, U_y, U_z. These functions are given explicitly in Appendix A.

Conical independent variables are introduced by the following transformation

$$\left.\begin{aligned} a_1 &= \sqrt{x^2 + y^2 + z^2} = x\lambda \\ b_1 &= \frac{y}{x} \\ c_1 &= \frac{z}{x} \end{aligned}\right\} \tag{2}$$

where $\lambda = \sqrt{1 + {b_1}^2 + {c_1}^2}$.

The conservation-law form of Equation 1 in this coordinate system is (14):

$$\begin{aligned} &\frac{\partial}{\partial t}\left(\frac{{a_1}^2}{\lambda^3} U\right) + \frac{\partial}{\partial a_1}\left\{\frac{{a_1}^2}{\lambda^4}\left[(E - E_v) + b_1(F - F_v) + c_1(G - G_v)\right]\right\} \\ &+ \frac{\partial}{\partial b_1}\left\{\frac{a_1}{\lambda^2}\left[-b_1(E - E_v) + (F - F_v)\right]\right\} \\ &+ \frac{\partial}{\partial c_1}\left\{\frac{a_1}{\lambda^2}\left[-c_1(E - E_v) + (G - G_v)\right]\right\} = 0 \end{aligned} \tag{3}$$

The assumption of local conical self-similarity requires that derivatives of all flow quantities be zero along rays passing through the apex of the wing

$$\frac{\partial E}{\partial a_1} = \frac{\partial E_v}{\partial a_1} = \frac{\partial F}{\partial a_1} = \frac{\partial F_v}{\partial a_1} = \frac{\partial G}{\partial a_1} = \frac{\partial G_v}{\partial a_1} = 0$$

This reduces the number of independent variables to three: time and two space variables. The calculations can be performed on a spherical surface centered at the apex. The viscous effects are scaled by the Reynolds number based on the radius of this surface, which is taken as reference length L.

Therefore $a_1 = 1$ and Equation 3 becomes

$$\frac{\partial}{\partial t}\left(\frac{U}{\lambda^3}\right) + \frac{\partial}{\partial b_1}\left[\frac{-b_1(E - E_v) + (F - F_v)}{\lambda^2}\right]$$

$$+ \frac{\partial}{\partial c_1}\left[\frac{-c_1(E - E_v) + (G - G_v)}{\lambda^2}\right]$$

$$+ \frac{2}{\lambda^4}\left[(E - E_v) + b_1(F - F_v) + c_1(G - G_v)\right] = 0 \qquad (4)$$

On the sphere $a_1 = 1$, it is useful to define a new set of independent variables by the generalized transformation

$$\left.\begin{aligned} \eta_1 &= \eta_1(t, b_1, c_1) \\ \zeta_1 &= \zeta_1(b_1, c_1) \end{aligned}\right\} \qquad (5)$$

whose Jacobian is defined as

$$\mathcal{D}_1 = \frac{\partial(\eta_1, \zeta_1)}{\partial(b_1, c_1)} = 1 \Big/ \frac{\partial(b_1, c_1)}{\partial(\eta_1, \zeta_1)} \qquad (6)$$

The final form of the governing equations in this new coordinate system is

$$\frac{\partial U_1}{\partial t} + \frac{\partial F_1}{\partial \eta_1} + \frac{\partial G_1}{\partial \zeta_1} + H_1 = 0 \tag{7}$$

where

$$U_1 = \frac{U}{\mathscr{D}_1 \lambda^3} \tag{8a}$$

$$F_1 = \frac{\partial \eta_1}{\partial t} U_1 - \frac{1}{\mathscr{D}_1 \lambda^2}\left(b_1 \frac{\partial \eta_1}{\partial b_1} + c_1 \frac{\partial \eta_1}{\partial c_1}\right)(E - E_V)$$

$$+ \frac{1}{\mathscr{D}_1 \lambda^2} \frac{\partial \eta_1}{\partial b_1} (F - F_V) + \frac{1}{\mathscr{D}_1 \lambda^2} \frac{\partial \eta_1}{\partial c_1} (G - G_V) \tag{8b}$$

$$G_1 = -\frac{1}{\mathscr{D}_1 \lambda^2}\left(b_1 \frac{\partial \zeta_1}{\partial b_1} + c_1 \frac{\partial \zeta_1}{\partial c_1}\right)(E - E_V)$$

$$+ \frac{1}{\mathscr{D}_1 \lambda^2} \frac{\partial \zeta_1}{\partial b_1} (F - F_V) + \frac{1}{\mathscr{D}_1 \lambda^2} \frac{\partial \zeta_1}{\partial c_1} (G - G_V) \tag{8c}$$

$$H_1 = \frac{2}{\mathscr{D}_1 \lambda^4} [(E - E_V) + b_1 (F - F_1) + c_1 (G - G_V)] \tag{8d}$$

The vectors E_V, F_V, G_V (see Appendix A) depend on U_x, U_y, U_z, which are given by

$$U_x = -\lambda\left(b_1 \frac{\partial \eta_1}{\partial b_1} + c_1 \frac{\partial \eta_1}{\partial c_1}\right) U_{\eta_1} - \lambda\left(b_1 \frac{\partial \zeta_1}{\partial b_1} + c_1 \frac{\partial \zeta_1}{\partial c_1}\right) U_{\zeta_1} \tag{9a}$$

$$U_y = \lambda \frac{\partial \eta_1}{\partial b_1} U_{\eta_1} + \lambda \frac{\partial \zeta_1}{\partial b_1} U_{\zeta_1} \tag{9b}$$

$$U_z = \lambda \frac{\partial \eta_1}{\partial c_1} U_{\eta_1} + \lambda \frac{\partial \zeta_1}{\partial c_1} U_{\zeta_1} \tag{9c}$$

The system of Equations 7 is mixed hyperbolic-parabolic in time; its steady state solution can be obtained with a time-dependent technique.

Grid Generation

The domain of computation on the sphere $a_1 = 1$ is limited by the bow shock and the body surface. Only one half of the flow field is considered; the other half is completed by symmetry.

The grid required for finite-difference calculations is shown in Figure 2, conically projected on the physical plane (y,z) at $x = 1$. Straight rays, making an angle α with the y axis, emanate from NJ grid points situated at the surface of the wing. Along each ray, within the distance δ between body and shock, NK points are positioned, which are clustered toward the wing surface.

The choice of the surface points and angles α is arbitrary, provided that they are regularly distributed. In the case of the delta wing, the surface points are clustered toward the wing tip. The shock standoff distance δ is determined by the shock boundary condition and is time dependent.

The generalized coordinates η_1 and ζ_1 are defined in such a way that in the computational plane (η_1,ζ_1) the grid has a square shape of side unity with uniform spacing in both directions. Therefore, the correspondence between physical and computational plane is, for $1 \leq j \leq NJ$ and $1 \leq k \leq NK$, the following:

$$\eta_1 = (k-1)\Delta\eta_1 \tag{10a}$$

$$\zeta_1 = (j-1)\Delta\zeta_1 \tag{10b}$$

and

$$y(j,k) = y_B(j) + s(i,j,\beta)\cos[\alpha(j)] \tag{11a}$$

$$z(j,k) = z_B(j) + s(i,j,\beta)\sin[\alpha(j)] \tag{11b}$$

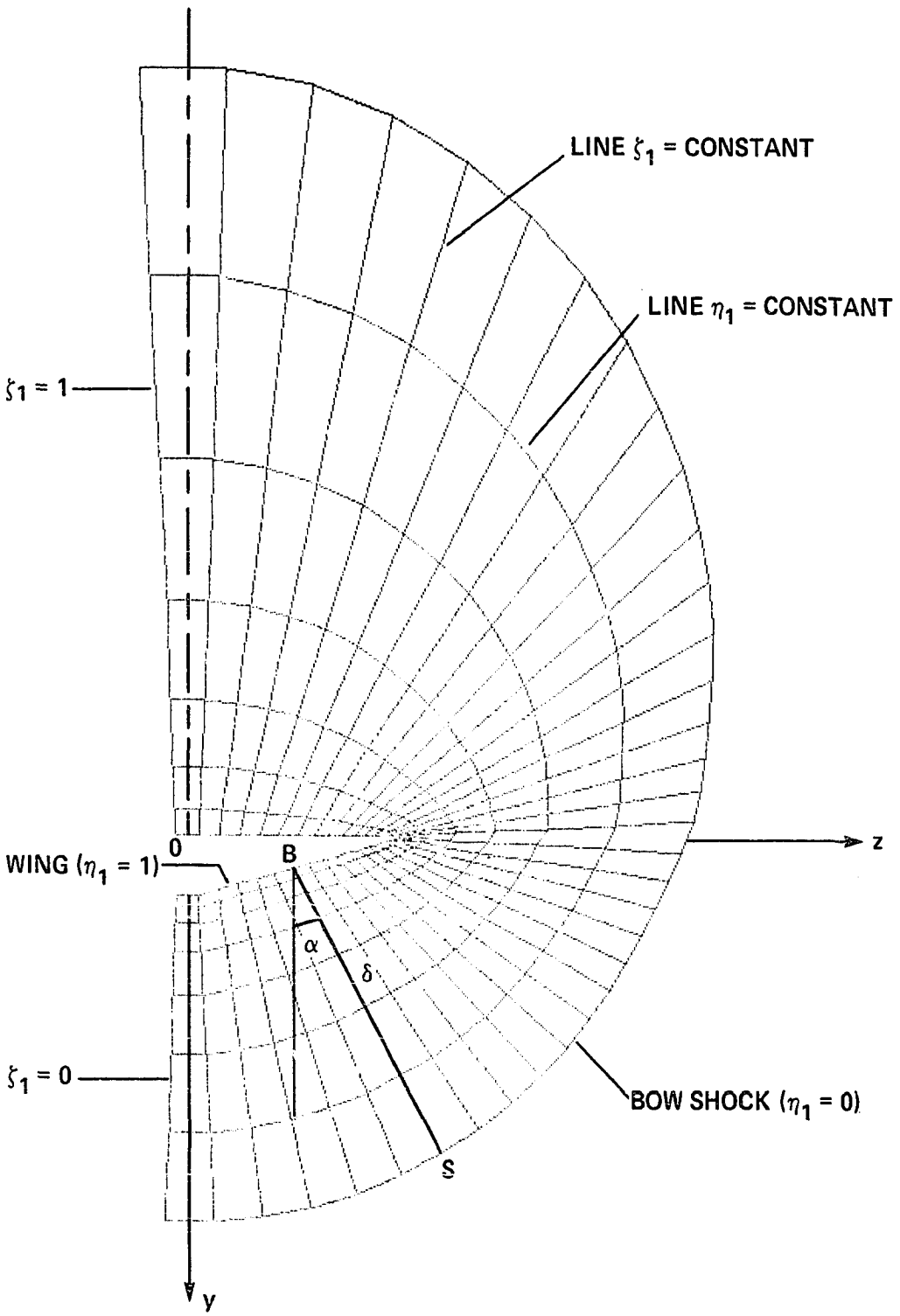

Figure 2. Grid distribution

where

$$\Delta\eta_1 = \frac{1}{NK-1}, \qquad \Delta\zeta_1 = \frac{1}{NJ-1}$$

and s is a stretching function (15) depending on η_1, δ, and a stretching parameter β

$$s(i,j,\beta) = \delta\left\{1-\beta\left[\left(\frac{\beta+1}{\beta-1}\right)^{\eta_1}-1\right]\Big/\left[1+\left(\frac{\beta+1}{\beta-1}\right)^{\eta_1}\right]\right\} \tag{11c}$$

Finally, the metrics $\partial\eta_1/\partial b_1$, $\partial\eta_1/\partial c_1$, $\partial\zeta_1/\partial b_1$, $\partial\zeta_1/\partial c_1$ are obtained from the relations

$$\left.\begin{aligned} \frac{\partial\eta_1}{\partial b_1} &= \mathscr{D}_1\frac{\partial c_1}{\partial\zeta_1} \qquad \frac{\partial\zeta_1}{\partial b_1} = -\mathscr{D}_1\frac{\partial c_1}{\partial\eta_1} \\ \frac{\partial\eta_1}{\partial c_1} &= -\mathscr{D}_1\frac{\partial b_1}{\partial\zeta_1} \qquad \frac{\partial\zeta_1}{\partial c_1} = \mathscr{D}_1\frac{\partial b_1}{\partial\eta_1} \\ \mathscr{D}_1 &= 1\Big/\left(\frac{\partial b_1}{\partial\eta_1}\cdot\frac{\partial c_1}{\partial\zeta_1}-\frac{\partial c_1}{\partial\eta_1}\cdot\frac{\partial b_1}{\partial\zeta_1}\right) \end{aligned}\right\} \tag{12}$$

where the derivatives $\partial b_1/\partial\eta_1$, $\partial b_1/\partial\zeta_1$, $\partial c_1/\partial\eta_1$, $\partial c_1/\partial\zeta_1$ are computed numerically with central difference operators in the regularly spaced computational plane (16,17).

Numerical Solution of Equations

Numerical algorithm

The governing equations are solved by a time-marching finite-difference technique. The computations are advanced in time, from a given initial condition, until a steady state is reached.

The numerical method is the standard, unsplit, explicit MacCormack (1969) predictor corrector algorithm (18) which has second-order accuracy in both time and space. A stability condition proportional to the grid

spacing restricts the maximum time increment. For the present viscous calculations, this time increment is computed using the empirical formula of Reference 19. Still, nonlinear instabilities, due to the very severe pressure gradient at the wing tip, were found to produce oscillations in the numerical solution. These oscillations were suppressed by using the fourth-order damping scheme introduced by MacCormack and Baldwin (20).

Each time step begins by the generation of new grid and the evaluation of the shock boundary condition. The finite-difference scheme is then implemented at each interior grid point. Finally all other boundary conditions are calculated.

Boundary conditions

The flow conditions at the shock boundary are computed by a "shock-fitting" technique. The Rankine Hugoniot relations are used across the shock which is allowed to move toward its steady-state position. A similar method was used and described in Reference 19 for a two-dimensional shock in body oriented coordinates. The extension to conical shocks in generalized coordinates is presented in Appendix B. Beside the flow properties, the shock stand-off distance and the metric coefficient $\partial\eta_1/\partial t$ are obtained.

Along the boundary $\zeta_1 = 0$ and $\zeta_1 = 1$, the flow variables and the geometric coefficients are determined using simple reflection about the plane of symmetry.

At the wall, the velocities are set to zero, the temperature is given, and the normal pressure gradient is assumed to be zero. This assumption is not justified at a sharp wing tip but the loss of accuracy is minimized by the fine cluster of mesh points in this region.

Initial conditions

The initial shock shape is an elliptic cone whose upper generator is a Mach line coming from the apex and whose lower generator is determined from a tangent-cone approximation. The initial shock speed is zero and the flow conditions behind the shock are obtained from the shock jump relations.

At the wall the temperature is known. The pressure on the leeward is approximated by a Prandtl Meyer expansion, and on the windward by cone theory.

At interior grid points, the flow variables are determined by assuming linear variation between the values behind the shock and those at the wall.

SECOND METHOD: PARABOLIC APPROXIMATION

Governing Equations

Two independent variable transformations are again applied to the general Navier-Stokes equations (Equation 1). They are similar to the transformations used for the conical approximation but allow for nonconical effects. The first transformation introduces conical coordinates

$$\left.\begin{aligned} a_2 &= x \\ b_2 &= \frac{y}{z} \\ c_2 &= \frac{z}{x} \end{aligned}\right\} \tag{13}$$

The second transformation allows for a stretched grid between arbitrary body and shock surfaces

$$\left.\begin{aligned} \xi_2 &= a_2 \\ \eta_2 &= \eta_2(a_2,b_2,c_2) \\ \zeta_2 &= \zeta_2(b_2,c_2) \end{aligned}\right\} \tag{14}$$

and

$$\mathcal{J}_2 = \frac{\partial(\eta_2,\zeta_2)}{\partial(b_2,c_2)}$$

At this point two assumptions are made:

1. Steady state $\partial/\partial t = 0$.

2. Viscous streamwise derivatives are negligible compared with the viscous normal and circumferential derivatives, that is, $\partial/\partial\xi_2 \equiv 0$ in the viscous terms only.

With these assumptions, the final form of the governing equations is

$$\left[\frac{\partial U_2}{\partial t}\right] + \frac{\partial E_2}{\partial \xi_2} + \frac{\partial F_2}{\partial \eta_2} + \frac{\partial G_2}{\partial \zeta_2} = 0 \tag{15}$$

where the unsteady term

$$U_2 = \frac{a_2{}^2 U}{\mathscr{D}_2} \tag{16a}$$

is only retained for further reference and

$$E_2 = \frac{a_2{}^2 E}{\mathscr{D}_2} \tag{16b}$$

$$F_2 = \frac{a_2}{\mathscr{D}_2}\left[\left(a_2\frac{\partial \eta_2}{\partial a_2} - b_2\frac{\partial \eta_2}{\partial b_2} - c_2\frac{\partial \eta_2}{\partial c_2}\right)(E - E_v) + \frac{\partial \eta_2}{\partial b_2}(F - F_v) + \frac{\partial \eta_2}{\partial c_2}(G - G_v)\right] \tag{16c}$$

$$G_2 = \frac{a_2}{\mathscr{D}_2}\left[\left(-b_2\frac{\partial \zeta_2}{\partial b_2} - c_2\frac{\partial \zeta_2}{\partial c_2}\right)(E - E_v) + \frac{\partial \zeta_2}{\partial b_2}(F - F_v) + \frac{\partial \zeta_2}{\partial c_2}(G - G_v)\right] \tag{16d}$$

The vectors E_v, F_v, G_v (see Appendix A) depend on U_x, U_y, U_z, which are given by

$$U_x = \frac{a_2\frac{\partial \eta_2}{\partial a_2} - b_2\frac{\partial \eta_2}{\partial b_2} - c_2\frac{\partial \eta_2}{\partial c_2}}{a_2} U_{\eta_2} + \frac{-b_2\frac{\partial \zeta_2}{\partial b_2} - c_2\frac{\partial \zeta_2}{\partial c_2}}{a_2} U_{\zeta_2} \tag{17a}$$

$$U_y = \frac{1}{a_2}\frac{\partial \eta_2}{\partial b_2} U_{\eta_2} + \frac{1}{a_2}\frac{\partial \zeta_2}{\partial c_2} U_{\zeta_2} \tag{17b}$$

$$U_z = \frac{1}{a_2}\frac{\partial \eta_2}{\partial b_2} U_{\eta_2} + \frac{1}{a_2}\frac{\partial \zeta_2}{\partial c_2} U_{\zeta_2} \tag{17c}$$

This system of equations is parabolic in the ξ_2 direction. It can be solved as an initial value problem.

At each station $x = \xi_2$, the generalized coordinates η_2 and ζ_2 are defined in such a way that the domain of computation, limited by the body surface, the bow shock and the plane of symmetry, is mapped into a square of side unity. The grid generation in the computational plane (η_2, ζ_2) is identical to the one described in the above subsection on grid generation. It can be noted that Equation 15 is valid for nonconical body shapes. However, for the conical shapes considered in this paper, $\partial \eta_2 / \partial a_2 = 0$ along the body surface. Therefore, the body grid points can be determined in terms of the coordinates b_2 and c_2 only, independent of $a_2 = x$.

Importance of the Streamwise Pressure Gradient

Previous analysis

If the initial value problem posed in the previous section is to be solved by forward integration in ξ_2, it is clear that no upstream influence can be allowed in the solution. It has been shown (21) that an exact representation of the streamwise pressure gradient p_{ξ_2} of Equation 15 causes information to be propagated upstream through the subsonic boundary layer close to the wall. Different remedies have been proposed with partial success. An obvious one is to drop altogether p_{ξ_2} from the equations. Cheng et al.(11)suggests evaluating p_{ξ_2} by a backward difference

and thus to introduce it as a source term. Some authors (12,13) have incorporated this idea in an iterative technique, to eventually approach the exact representation. Rubin and Lin (12) have also proposed a "sub-layer approximation" where the term p_{ξ_2} for the subsonic region is calculated at a supersonic point outside the boundary layer.

Numerical results for each procedure are given in Reference 12 for a two-dimensional hypersonic leading-edge problem. Except for the approximation $p_{\xi_2} = 0$, all the methods tend to exhibit instabilities and produce what is known as departure solutions, with a separation-like increase in wall pressure, or an expansion-like decrease in wall pressure. Lubard and Helliwell (13) have performed a stability analysis of their numerical scheme when applied to a similar system of equations. They find that the step size Δ_{ξ_2} must be greater than some minimum to avoid departure solutions. This trend was verified by their numerical experimentation.

Present analyses

A new way of looking at this problem is to determine the influence of the streamwise pressure gradient on the mathematical nature of the equations through an eigenvalue analysis. For this, consider the two-dimensional parabolized Navier-Stokes equation on a flat plate, assuming constant velocity. A parameter ω is introduced so that these equations are written as

$$\frac{\partial E^*}{\partial x} + \frac{\partial P}{\partial x} + \frac{\partial F}{\partial y} = \frac{\partial F_v}{\partial y} \tag{18}$$

where

$$E^* = \begin{bmatrix} \rho u \\ \rho u^2 + \omega p \\ \rho uv \\ \left[\frac{\gamma}{\gamma - 1} p + \frac{\rho}{2} (u^2 + v^2)\right] u \end{bmatrix} \qquad P = \begin{bmatrix} 0 \\ (1 - \omega) p \\ 0 \\ 0 \end{bmatrix}$$

$$F = \begin{bmatrix} \rho u \\ \rho uv \\ \rho v^2 + p \\ \left[\frac{\gamma}{\gamma - 1} p + \frac{\rho}{2} (u^2 + v^2)\right] v \end{bmatrix}$$

$$F_v = \frac{\mu}{Re} \begin{bmatrix} 0 \\ u_y \\ \frac{4}{3} v_y \\ uu_y + \frac{4}{3} vv_y + \frac{Ty}{(\gamma - 1) M_\infty^2 Pr} \end{bmatrix} \qquad (19)$$

In this formulation $\partial P/\partial x$ is to be treated as a source term with a backward difference. The problem is to determine what proportion ω of p_x can be taken out of the source term $\partial P/\partial x$ and included in E^* without causing upstream influence. The inviscid limit is considered first ($Re \to \infty$)

$$\frac{\partial E^*}{\partial x} + \frac{\partial F}{\partial y} = 0 \qquad (20)$$

Except for the ωp_x term, these are the Euler equations which can be written also as

$$A_1 Q_x + B_1 Q_y = 0 \qquad (21)$$

where

$$Q = \begin{bmatrix} \rho \\ u \\ v \\ p \end{bmatrix} \quad A_1 = \begin{bmatrix} u & \rho & 0 & 0 \\ 0 & \rho u & 0 & \omega \\ 0 & 0 & \rho u & 0 \\ -a^2 u & 0 & 0 & u \end{bmatrix} \quad B_1 = \begin{bmatrix} v & 0 & \rho & 0 \\ 0 & \rho v & 0 & 0 \\ 0 & 0 & \rho v & 1 \\ -a^2 v & 0 & 0 & v \end{bmatrix} \tag{22}$$

and a is the speed of sound. These equations are hyperbolic in x and can be integrated forward in x if the eigenvalues of $(A_1^{-1} \cdot B_1)$ are real. These eigenvalues are

$$\lambda_{1,2} = \frac{v}{u} \tag{23a}$$

$$\lambda_{3,4} = \frac{uv \pm a\sqrt{u^2 + \omega(v^2 - a^2)}}{u^2 - \omega a^2} \tag{23b}$$

and they are real if

$$\omega < \frac{u^2}{a^2 - v^2} = \frac{M_x^2}{1 - \frac{v^2}{a^2}} \tag{24}$$

where $M_x = u/a$.

Therefore, in the region where $M_x > 1$, the p_x term can be included fully in E^* but it must be restricted according to Equation 24 where $M_x < 1$. It is only in the incompressible limit, $M_x \to 0$, that the entire pressure gradient must be in the source term.

Next, the viscous limit is considered and the first derivatives with respect to y are neglected from Equation 18. In this case

$$A_2 Q_x = B_2 Q_{yy} \tag{25}$$

where:

$$A_2 = \begin{bmatrix} u & \rho & 0 & 0 \\ u^2 & 2\rho u & 0 & \omega \\ uv & \rho v & \rho u & 0 \\ u\dfrac{u^2+v^2}{2} & \dfrac{\gamma p}{\gamma-1}+\dfrac{\rho(3u^2+v^2)}{2} & \rho uv & \dfrac{\gamma u}{\gamma-1} \end{bmatrix}$$

$$B_2 = \frac{\mu}{Re}\begin{bmatrix} 0 & 0 & 0 & 0 \\ 0 & 1 & 0 & 0 \\ 0 & 0 & \frac{4}{3} & 0 \\ -\dfrac{\gamma p}{(\gamma-1)Pr\rho^2} & u & \dfrac{4v}{3} & \dfrac{\gamma}{(\gamma-1)Pr\rho} \end{bmatrix} \tag{26}$$

These equations are parabolic in the positive x direction if the eigenvalues of $(A_2^{-1} \cdot B_2)$ are real and positive. The eigenvalues are given by the zeros of the following polynomial (assuming $u \neq 0$)

$$\lambda\left(Re\,\frac{\rho u}{\mu}\,\lambda - \frac{4}{3}\right)\left[\left(Re\,\frac{\rho u}{\mu}\,\lambda\right)^2\left\{M_x^2[\gamma - \omega(\gamma-1)] - \omega\right\} + \left(Re\,\frac{\rho u}{\mu}\,\lambda\right)\left\{\left[\omega(\gamma-1) - \gamma\,\frac{1+Pr}{Pr}\right]M_x^2 + \frac{\omega}{Pr}\right\} + \frac{\gamma M_x^2}{Pr}\right] \tag{27}$$

One can show that they will be real and positive if

$$u > 0 \tag{28a}$$

and

$$\omega < \frac{\gamma M_x^2}{1 + (\gamma-1)M_x^2} = f^*(M_x) \tag{28b}$$

The function $f^*(M_x)$ has the property that $f^*(1) = 1$ and $f^*(M_x) > 1$ for $M_x > 1$. So that again, if $M_x > 1$ the term p_x can be included fully in E^*, but must be restricted according to Equation 28b if $M_x < 1$. Equation 28a forbids reverse flows.

In the present code, ω is computed at each point once the flow variables are known. The equation for ω is

$$\left.\begin{aligned} \omega &= \sigma f^*(M_x) \quad \text{if} \quad \sigma f^*(M_x) \leq 1 \\ \omega &= 1 \quad \text{if} \quad \sigma f^*(M_x) \geq 1 \end{aligned}\right\} \tag{29}$$

where σ is a safety factor.

The source term $\partial P/\partial x$ has not been taken into account in this analysis. It can be evaluated using a backward difference based either on the local pressure gradient, or on the pressure gradient outside the subsonic layer at a point where $M_x = M_{x_e} > 1$. However, the following section shows that if a backward difference based on the local pressure gradient is used, the source term $\partial P/\partial x$ can have a critical influence on the stability of the solution, and thus may have to be dropped.

Linear stability analysis

In this section, the two-dimensional parabolized Navier-Stokes equations (Equation 18) are marched in the x direction with the Euler implicit scheme, and a linear stability analysis of the resulting difference equations is performed to determine which conditions must be satisfied by the step size Δx to obtain relaxation solutions. These conditions on Δx will prohibit solutions with exponential growth caused either by numerical instabilities or departure behavior. Again, only the viscous limit of Equations 18 is considered, but the source term $\partial P/\partial x$ is now included.

(Recall that this term represents the explicit part of the pressure gradient, that is, $(1 - \omega)p_x$.) This system of equations can be written as:

$$E_U^* \frac{\partial U}{\partial x} + P_U \frac{\partial U}{\partial x} = F_{V_{U_y}} \frac{\partial^2 U}{\partial y^2} \tag{30}$$

where

$$U = \begin{bmatrix} \rho \\ \rho u \\ \rho v \\ \rho\left(e + \dfrac{u^2 + v^2}{2}\right) \end{bmatrix}$$

and E_U^*, P_U, $F_{V_{U_y}}$ represent the Jacobians $\partial E^*/\partial U$, $\partial P/\partial U$, $\partial F_y/\partial U_y$.

If the Euler implicit scheme is applied to Equation 30 and the $\partial P/\partial x$ is evaluated with a local backward difference, the difference equations are:

$$E_U^* \frac{U_j^{i+1} - U_j^{i}}{\Delta x} + P_U \frac{U_j^{i} - U_j^{i-1}}{\Delta x} = F_{V_{U_y}} \frac{U_{j+1}^{i+1} - 2U_j^{i+1} + U_{j-1}^{i+1}}{\Delta y^2} \tag{31}$$

or

$$\left(E_U^* + 2\phi F_{V_{U_y}}\right) U_j^{i+1} - \phi F_{V_{U_y}} \left(U_{J+1}^{i+1} + U_{J-1}^{i+1}\right) + (P_U - E_U^*)U_j^{i} - P_U U_j^{i-1} = 0 \tag{32}$$

where

$$\phi = \frac{\Delta x}{\Delta y^2}$$

and the index i refers to the x direction and the index j to the y direction.

In order to obtain a relaxing solution, the eigenvalues of the associated amplification matrix must have a modulus less than unity. The

coefficient matrix (13) is obtained by replacing in Equation 32 U_j^i by $\tilde{U}\exp(\sqrt{-1}Kj\,\Delta y)$ and $U_j^{i\pm1}$ by $\lambda^{\pm1}\tilde{U}\exp(\sqrt{-1}K\,\Delta y)$. The eigenvalues of the amplification matrix are the values of λ for which the determinant of the coefficient matrix vanishes.

$$\det\left\{\lambda^2[E_U^* - 2\phi F_{V_{U_y}}(\cos K\Delta y - 1)] + \lambda(P_U - E_U^*) - P_U\right\} = 0 \tag{33}$$

Equation 33 is a polynomial of degree 8 in λ. If the normal velocity v is neglected and u is assumed to be nonzero, it can be shown that this polynomial can be written as

$$\lambda^3 \cdot (\lambda - 1) \cdot \mathcal{B}(\lambda,X) \cdot \mathcal{C}(\lambda,X,M_x,\omega) = 0 \tag{34}$$

where

$$\mathcal{B}(\lambda,X) \equiv \left(1 + \frac{4}{3}X\right)\lambda - 1 \tag{35}$$

and

$$\begin{aligned}\mathcal{C}(\lambda,X,M_x,\omega) \equiv {} & \left\{\lambda^2\left[\frac{\omega(\gamma-1)-2}{2} - X\right] + \lambda\left[\frac{\gamma+1-2\omega(\gamma-1)}{2}\right] - \frac{(1-\omega)(\gamma-1)}{2}\right\} \\ & \cdot \left\{\left[\gamma + \frac{\gamma}{Pr}X\right]\lambda - \gamma\right\} - (\gamma-1)[\omega\lambda^2 + (1-2\omega)\lambda - (1-\omega)] \\ & \cdot \left\{\lambda\left[\frac{\gamma - 2 + X\,\frac{\gamma}{Pr} - 2}{2} - \frac{Pr + X}{Pr(\gamma-1)M_x^2}\right] + \frac{1}{(\gamma-1)M_x^2} - \frac{\gamma-2}{2}\right\}\end{aligned} \tag{36}$$

and

$$X = \frac{4\mu\Delta x}{\rho u Re \Delta y^2}\sin^2\left(\frac{K\Delta y}{2}\right) \tag{37}$$

Equation 34 has five obvious roots

$$\lambda = 0 \text{ (triple root)}$$

$$\lambda = 1 \tag{38}$$

$$\lambda = \frac{1}{1 + \frac{4}{3} X}$$

If $u > 0$, then $X > 0$ and these five eigenvalues always have a modulus less or equal to one, thus providing unconditional (neutral) stability.

The remaining eigenvalues are the roots of the polynomial of the third degree $\mathscr{C}(\lambda, X, M_X, \omega)$. This equation is difficult to handle analytically. Therefore a numerical parametric study was performed. For discrete values of X, M_X, ω such that:

$$\left.\begin{aligned} X &> 0 \\ M_X &> 0 \\ 0 < \omega &< 1 \end{aligned}\right\}$$

A numerical procedure was used to find the real and complex roots of $\mathscr{C}(\lambda, X, M_X, \omega)$. This procedure is a Newton-Raphson iterative technique where the final iteration on each root utilizes the original polynomial rather than the reduced polynomial to avoid accumulated errors in the reduced polynomial.

From these numerical calculations, the following conclusions can be drawn

(1) if $M_X > 1$

$|\lambda| < 1$ for all $X > 0$ and $0 \leq \omega \leq 1$

(2) if $M_X < 1$ and $\frac{\partial P}{\partial x}$ is dropped from Equation 30

$|\lambda| \leq 1$ for all $X > 0$ and $0 \leq \omega \leq f^*(M_X)$

(It is important to note that conclusions (1) and (2) provide an independent check of the results obtained in the previous subsection)

(3) if $M_x < 1$ and $\frac{\partial P}{\partial x}$ is dropped from Equation 30

and $f^*(M_x) < \omega \leq 1$ then $|\lambda| \leq 1$ only if $X > \bar{X}_{min}(\omega, M_x)$

(4) if $M_x < 1$ and $\frac{\partial P}{\partial x}$ is included in Equation 30

and $0 \leq \omega \leq 1$

then $|\lambda| \leq 1$ only if $X > \bar{\bar{X}}_{min}(\omega, M_x)$

These results are consistent with those of Lubard and Helliwell (13) who studied the two cases $\omega = 0$ and $\omega = 1$ and found that

(1) if $M_x > 1$ and $\omega = 0$ or $\omega = 1$

$|\lambda| \leq 1$ for all $X > 0$

(2) if $M_x < 1$ and $\frac{\partial P}{\partial x}$ is dropped from Equation 30

and $\omega = 0$

$|\lambda| \leq 1$ for all $X > 0$

(3) if $M_x < 1$ and $\frac{\partial P}{\partial x}$ is included in Equation 30

and $\omega = 0$

then $|\lambda| \leq 1$ only if

$$X > \frac{1 - M_x^2}{\gamma M_x^2} \tag{39}$$

(4) if $M_x < 1$ and $\omega = 1$

then $|\lambda| \leq 1$ only if

$$X > \frac{2(1 - M_x^2)}{\gamma M_x^2} \tag{40}$$

Figures 3-6 illustrate these conclusions. In these figures, the modulus of the largest root of the polynomial $\mathscr{C}(\lambda)$ is plotted versus the

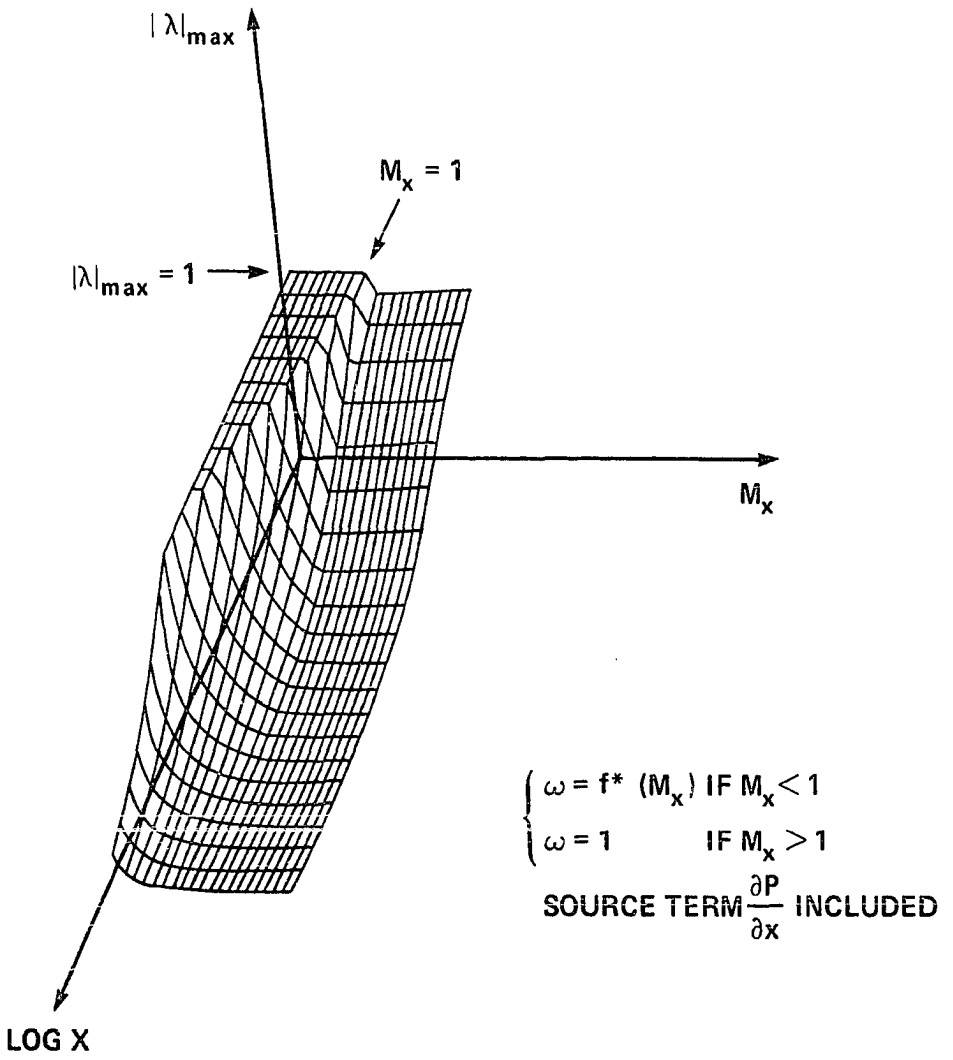

Figure 3. Domain of stability for $\omega = f^*(M_x)$

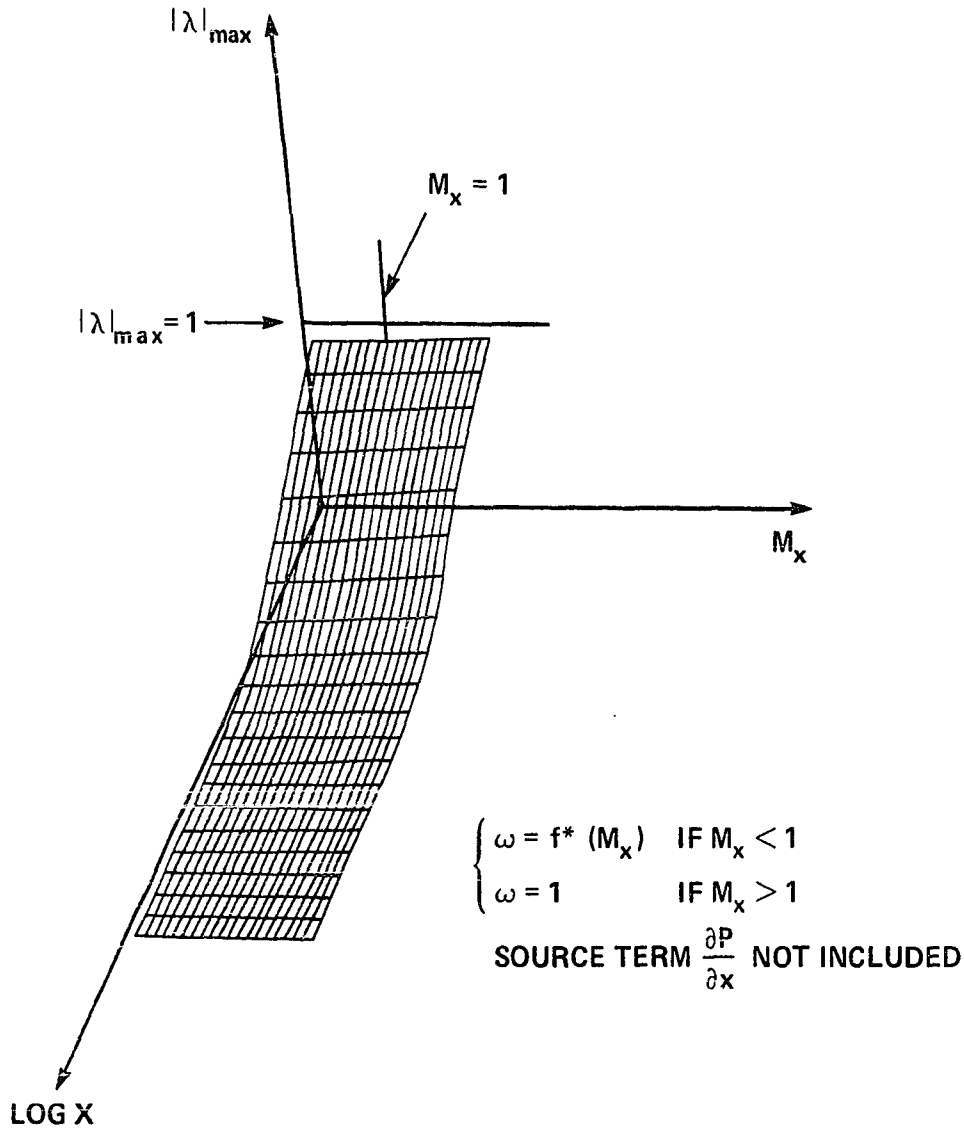

Figure 4. Domain of stability for $\omega = f^*(M_x)$ and no source term $\frac{\partial P}{\partial x}$

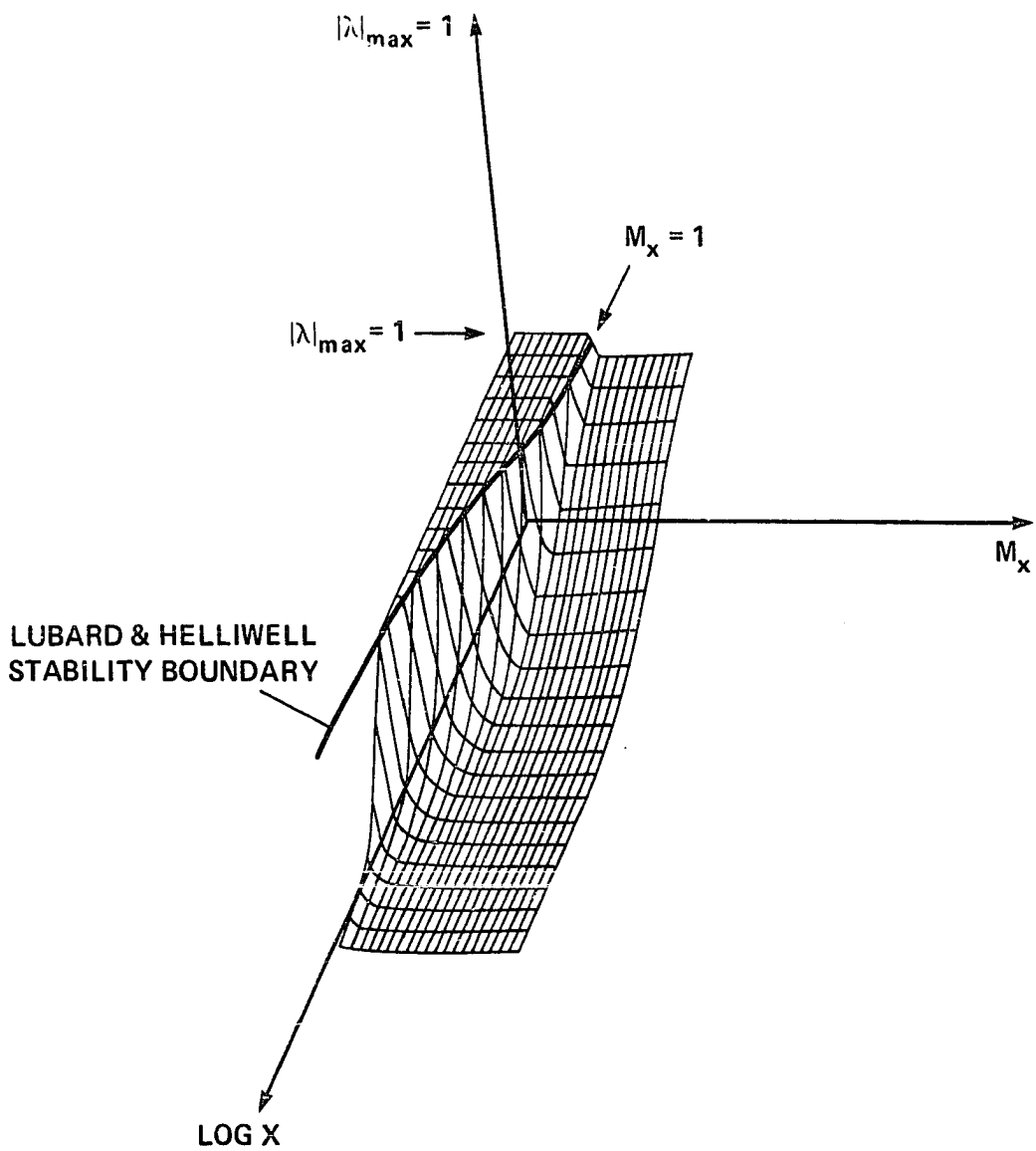

Figure 5. Domain of stability for $\omega = 1$

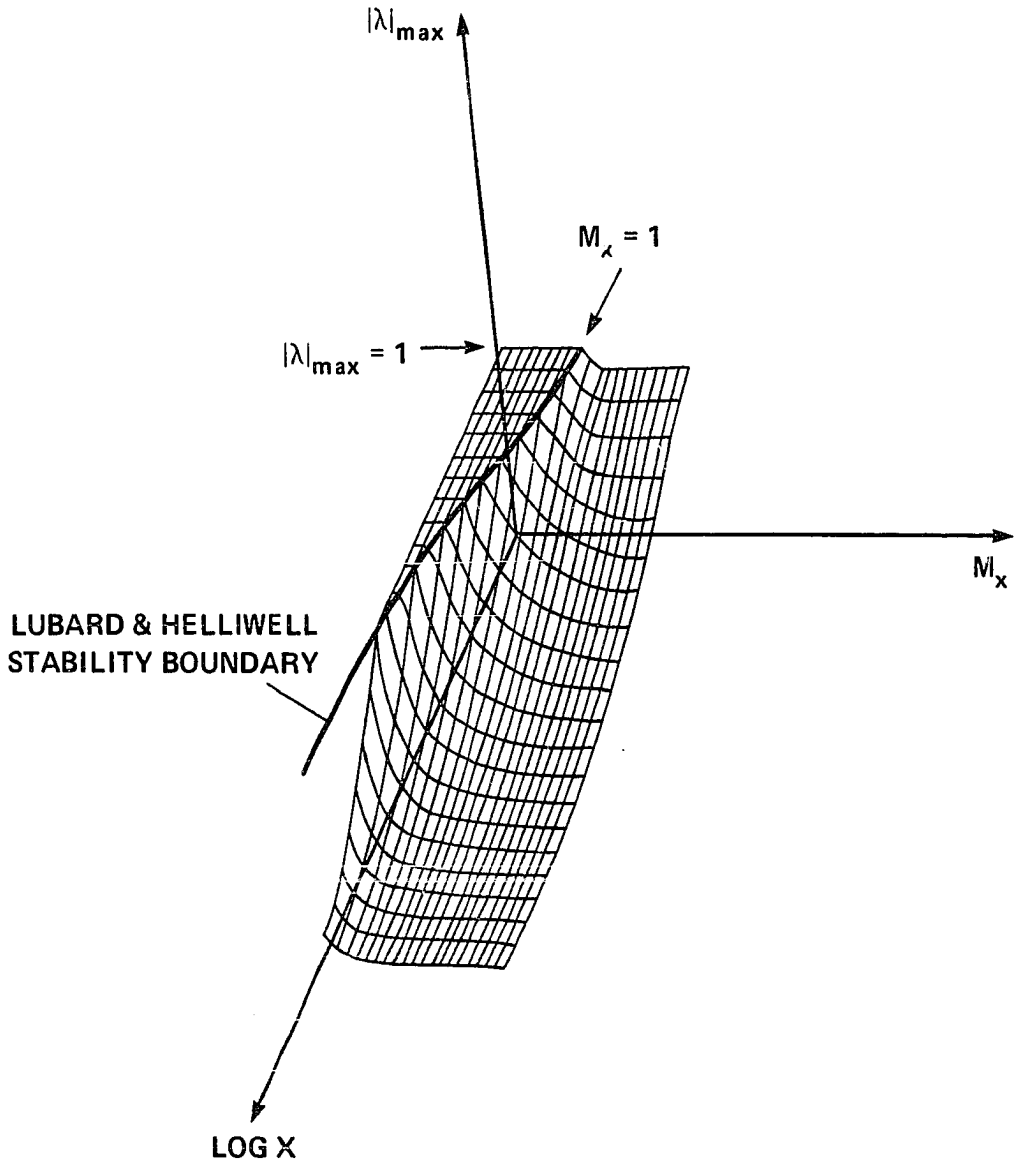

Figure 6. Domain of stability for $\omega = 0$ and source term $\frac{\partial P}{\partial x}$ included.

parameters M_x and Log X, for fixed values of ω. If the modulus of the largest root is greater than one, the plotting routine sets it equal to one. With this procedure, the regions of instability are represented by a flat surface which is easy to detect.

Figures 3 and 4 illustrate the role of the pressure gradient on stability. Here the parameter ω is determined by Equation 29:

$$\left.\begin{array}{ll} \text{If} \quad M_x < 1 & \omega = f^*(M_x) \\ \text{If} \quad M_x > 1 & \omega = 1 \end{array}\right\} \tag{41}$$

In Figure 3 the source term $\partial P/\partial x$ is included and there is a region of instability for small X and M_x. If the source term $\partial P/\partial x$ is dropped (Figure 4), this region of instability disappears. Figures 5 and 6 compare the results of the present analysis with those of Lubard and Helliwell. In Figure 5 the parameter ω is set equal to one (completely implicit pressure gradient). Again, there is an unstable region at small X and M_x. The limit of this unstable region, as determined by Lubard and Helliwell (Equation 40) is also shown. It is clear that both analyses agree very well. This is also true for the case $\omega = 0$ (completely explicit pressure gradient) as can be seen in Figure 6.

At this point, it is necessary to look at the physical meaning of the existence of a minimum value for the parameter X. The analysis of this section is a viscous analysis, therefore strictly valid only for the first point off the wall boundary. This point is situated at a distance Δy above the wall. For simplicity, the boundary condition at the wall can be taken as a Dirichlet boundary condition (fixed U_{wall}). Then the numerical solution of the difference Equation 32 will generate a round-off error

whose dominant harmonic is likely to have a period of $4\Delta y$. If only this harmonic is considered, then

$$K = \frac{\pi}{2\Delta y} \tag{42}$$

and

$$X = \frac{2\mu\ \Delta x}{\rho u Re\ \Delta y^2} \tag{43}$$

The condition

$$X > X_{min}$$

is equivalent to imposing a lower bound on the marching step. In particular, if the mesh Reynolds number, $Re = (\rho u\ \Delta y)/\mu$, is taken as unity for accuracy purpose, it turns out that:

$$2\ \frac{\Delta x}{\Delta y} > X_{min} \tag{44}$$

This unusual stability condition has been verified experimentally by Lubard and Helliwell (13). Unlike Reference 13, the present analysis does not provide an analytical formula for the lower bound on Δx. However, this is not so restrictive since in a real problem, the minimum Δx has to be determined by trial and error.

As a conclusion, it is important to recall the main result of the present analysis: the best strategy to obtain unconditional stability is to include only part of the pressure gradient in the normal implicit algorithm — namely, ωp_x where ω is given by Equation 41 — and drop the other part entirely, that is, $(1 - \omega)p_x$.

Numerical Solution of Equations

Numerical algorithm

Equation 15 is solved with a finite-difference technique adapted from the class of completely implicit, noniterative ADI schemes introduced by Lindemuth and Killeen (22), Briley and MacDonald (23,24), and Beam and Warming (25-27). It uses the implicit approximate factorization in delta form of Beam and Warming (26). The choice of an implicit algorithm is justified when the limit imposed on the marching step by the stability condition of an explicit method is smaller than the limit required for accuracy. This is the case of the delta wing at angle of attack where the gradients in the longitudinal marching direction are very small compared to the large normal gradients due to viscosity and the large lateral gradients near the tip of the wing. Moreover the noniterative character of the present method is expected to provide better efficiency than the iterative schemes of Rubin and Lin (12) and Lubard and Helliwell (13).

For the governing Equation 15, written as

$$\frac{\partial \hat{E}_2^*}{\partial \xi_2} + \frac{\partial P_2}{\partial \xi_2} + \frac{\partial F_2}{\partial \eta_2} + \frac{\partial G_2}{\partial \zeta_2} = 0 \tag{45}$$

the delta form of the algorithm for constant step size $\Delta\xi_2$ is

$$\left[\frac{\partial E_2^*}{\partial U_2} + \frac{\theta_1 \Delta\xi_2}{1+\theta_2} \frac{\partial}{\partial \zeta_2}\left(\frac{\partial G_2}{\partial U_2}\right)\right]\left(\frac{\partial E_2^*}{\partial U_2}\right)^{-1}$$
$$\times \left[\frac{\partial E_2^*}{\partial U_2} + \frac{\theta_1 \Delta\xi_2}{1+\theta_2} \frac{\partial}{\partial \eta_2}\left(\frac{\partial F_2}{\partial U_2}\right)\right] \Delta^i U_2$$
$$= -\frac{\Delta\xi_2}{1+\theta_2}\left(\frac{\partial F_2}{\partial \eta_2} + \frac{\partial G_2}{\partial \zeta_2}\right)^i + \frac{\theta_2}{1+\theta_2} \Delta^{i-1} E_2 - \Delta_e P_2 \tag{46}$$

where the superscript i refers to the level $\xi_2 = i\Delta\xi_2$ and $U_2 = a_2{}^2U/\mathcal{D}_2$ (unsteady term of Equation 15) and

$$\Delta^i U_2 = U_2^{i+1} - U_2{}^i$$

and the derivatives ∂_{η_2} and ∂_{ζ_2} are approximated with central difference operators.

This algorithm has been factorized in terms of U_2 rather than E_2^* because the computation of the Jacobians $\partial F_2/\partial U_2$, $\partial G_2/\partial U_2$ is easier than the computation of $\partial F_2/\partial F_2$, $\partial G_2/\partial E_2^*$. Since the vectors E, F, G are homogeneous functions of degree one in U, the conservative form of the governing equations is maintained.

For first-order accuracy in ξ_2, the Euler implicit scheme is used ($\theta_1 = 1$, $\theta_2 = 0$). The Jacobians are evaluated at level i and $\Delta_e P = \Delta^{i-1}P$. If second-order accuracy in ξ_2 is desired, one can use the Crank-Nicolson scheme ($\theta_1 = 1/2$, $\theta_2 = 0$) or the three-points backward implicit scheme ($\theta_1 = 1$, $\theta_2 = 1/2$). In this case, the Jacobians should be evaluated at $i = (1/2)$; this can be done through an extrapolation of levels i and $i-1$. Also $\Delta_e P = 2\Delta^{i-1}P - \Delta^{i-2}$. In this study, only results obtained with the first-order scheme will be presented.

The complete definition of the Jacobians is given in Appendix C. Two approximations are made in the computation of the viscous Jacobians. The coefficient of molecular viscosity is assumed to depend only on the position, not on the vector U. And, consistent with first-order computations, the cross derivative viscous terms in the (η_2,ζ_2) plane are neglected from the Jacobians.

In practice, algorithm 46 is implemented as follows:

$$\left.\begin{aligned}
\left[\frac{\partial E_2^*}{\partial U_2} + \frac{\theta_1 \Delta\xi_2}{1+\theta_2}\frac{\partial}{\partial \zeta_2}\left(\frac{\partial G_2}{\partial U_2}\right)\right]\Delta\bar{U}_2 &= \text{RHS(31)} \\
\Delta\bar{\bar{U}}_2 &= \frac{\partial E_2^*}{\partial U_2}\Delta\bar{U}_2 \\
\left[\frac{\partial E_2^*}{\partial U_2} + \frac{\theta_1 \Delta\xi_2}{1+\theta_2}\frac{\partial}{\partial \eta_2}\left(\frac{\partial F_2}{\partial U_2}\right)\right]\Delta^i U_2 &= \Delta\bar{\bar{U}}_2 \\
U_2^{i+1} &= U_2{}^i + \Delta^i U_2
\end{aligned}\right\} \qquad (47)$$

Each one-dimensional operator corresponds to a block-tridiagonal system of equations. In the present computations these systems are solved with a routine written by J. L. Steger and described in Reference 17.

The numerical stability of the implicit portion of algorithm 46 has been studied by Beam and Warming for simple hyperbolic and parabolic model equations (27). Applied to those model equations, the Euler implicit scheme ($\theta_1 = 1/2$, $\theta_2 = 0$) is unconditionally stable.

Finally, some artificial dissipation is added to the basic scheme 46. Fourth-order dissipation terms are added explicitly to damp eventual high-frequency oscillations of the solutions. These fourth-order terms are either identical to those used by Beam and Warming (26) and by Steger (17) or similar to the MacCormack damper of the conical approximation. Also, some second-order implicit dissipation is used. This idea, introduced to improve the stability of time-marching solvers (28), is used here to prevent departure solutions and to initiate the calculations. Its truncation error is consistent with a first-order Euler scheme.

The final algorithm is therefore (with the fourth-order explicit smoothing of Reference 26)

$$\left[\frac{\partial E_2^*}{\partial U_2} + \frac{\theta_1 \Delta\xi_2}{1+\theta_2}\,\partial_{\zeta_2}\left(\frac{\partial G_2}{\partial U_2}\right) - \varepsilon_I \mathscr{D}_2^{-1}\nabla_{\zeta_2}\Delta_{\zeta_2}\mathscr{D}_2\right]\left(\frac{\partial E_2^*}{\partial U_2}\right)^{-1}$$

$$\times\left[\frac{\partial E_2^*}{\partial U_2} + \frac{\theta_1 \Delta\xi_2}{1+\theta_2}\,\partial_{\eta_2}\left(\frac{\partial F_2}{\partial U_2}\right) - \varepsilon_I \mathscr{D}_2^{-1}\nabla_{\eta_2}\Delta_{\eta_2}\mathscr{D}_2\right]\Delta^i U_2$$

$$= -\frac{\Delta\xi_2}{1+\theta_2}\left(\frac{\partial F_2}{\partial \eta_2} + \frac{\partial G_2}{\partial \zeta_2}\right)^i + \frac{\theta_2}{1+\theta_2}\,\Delta^{i-1}E_2 - \Delta_e P$$

$$- \varepsilon_E \mathscr{D}_2^{-1}\left[\left(\nabla_{\eta_2}\Delta_{\eta_2}\right)^2 + \left(\nabla_{\zeta_2}\Delta_{\zeta_2}\right)^2\right]\mathscr{D}_2 U_2{}^i \qquad (48)$$

where ∇ and Δ are the conventional forward and backward difference operators and ε_E and ε_I are the coefficients of explicit and implicit dissipation.

Boundary conditions

The conditions at the shock boundary are computed by a "shock fitting" technique for steady-state supersonic flows due to Thomas et al. (29). Details of the procedure can be found in Appendix B. The required pressure behind the shock is determined by an implicit one-sided integration of the governing Equation 15. Because this technique is not truly implicit, it puts a limit on the allowed integration step size $\Delta\xi_2$. This limit is much larger than the one which would be imposed by an explicit stability condition near the wall. However, it can be smaller than the minimum step size required to include the source term $\partial P_2/\partial\xi_2$ (see the linear stability analysis of the previous section). In this eventuality, the source term has to be dropped.

At the body surface, the change of the conservative variables $\Delta^i U_{2_{j,k=NK}}$ is extrapolated from the previous value $\Delta^{i-1} U_2$ and then used as known boundary condition in the solution of each one-dimensional normal operator of algorithm 46. Once the flow variables have been found at the interior grid points, the surface values are computed as in the conical approximation. The velocities are set to zero, the temperature is given, and the normal pressure gradient is assumed to be zero.

The plane-of-symmetry boundary conditions are computed by reflection and they are imposed implicitly.

Initial conditions

In addition to the boundary conditions, some initial conditions are necessary. Ideally, the region near the apex of the wing should be computed with the full Navier-Stokes equations. In the present study the conical approximation described in Section II is used to generate a starting solution. The calculations are then advanced downstream to a station ξ_2 where they are compared with another conical solution and with available experimental data.

RESULTS AND DISCUSSION

Test Conditions

Laminar calculations have been performed for three test cases. A description of the test conditions is given in Table 1. The first case is a circular cone, at angle of attack, for which experimental as well as numerical results are available. It provides a good evaluation of each procedure described in the previous sections before considering the delta wings of cases No. 2 and No. 3.

Table 1. Test conditions

	Test case 1	Test case 2	Test case 3
Experiment	Tracy (30)	Monnerie and Werlé (7)	Thomann (8)
Body shape	Circular cone	Delta wing	Delta wing
Half angle or sweep	10°	75°	75.7°
Angle of attack	24°	10°	9.5°
M_∞	7.95	1.95	3.04
Re_L	0.42×10^6	0.76×10^6	10^6
T_{wall}/T_∞	5.59	1.13	3

Results from the Conical Approximation

Test case No. 1

For the cone calculations the mesh had 20 points along the surface and 31 across the shock layer. The constant-ζ rays were chosen normal to the surface with a spacing of 10°. The stretching parameter β was set equal to 1.12. The results are compared with the experimental data of Tracy (30) and the numerical calculations of McRae (9).

Figure 7 shows a crosscut of the cone, the shock shapes and the tangential conical cross-flow velocity contours. Outlined is the zone of reverse crossflow. The agreement between experiment and computations is

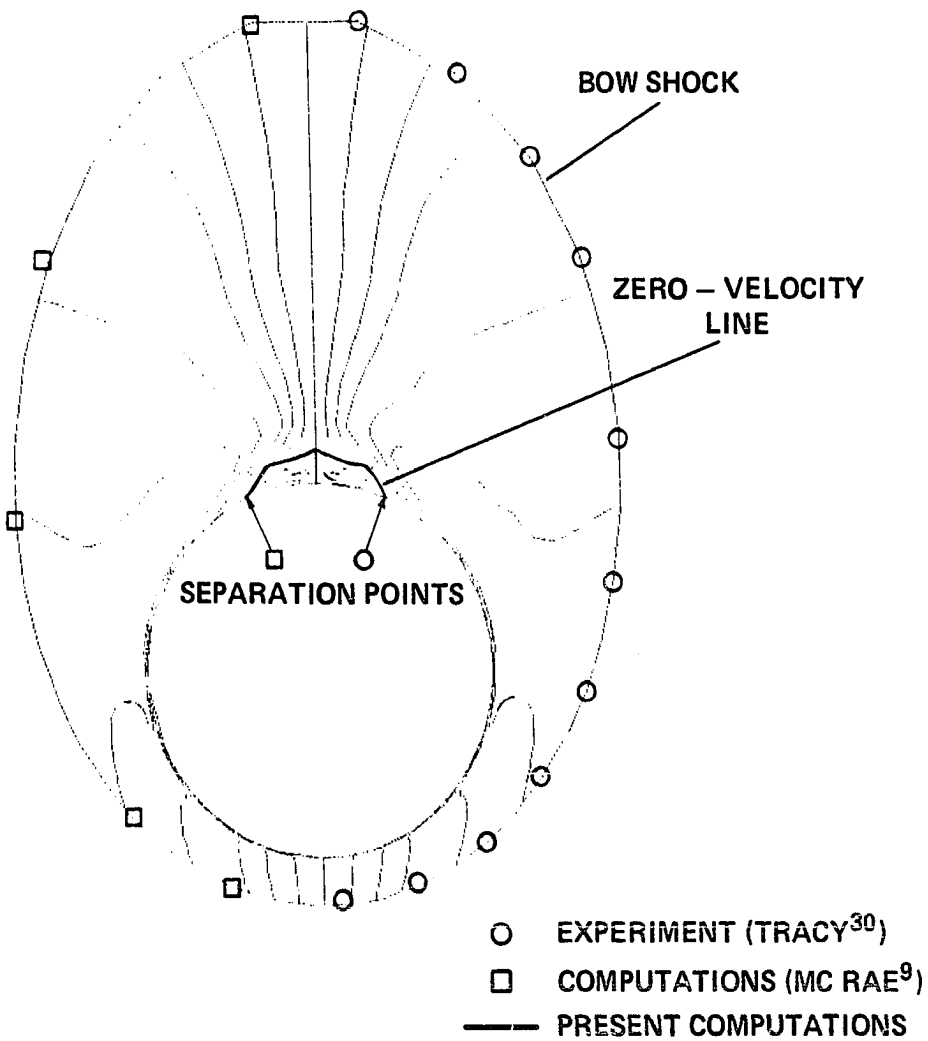

Figure 7. Test case No. 1 — conical approximation cross-flow velocity contours

excellent, for the shock shape as well as the separation point. The surface pressure distributions are given in Figure 8. Also presented is the surface pressure computed with the conical approximation at a station situated at 20% of the length of the cone ($Re_L = 0.84\times10^5$). It is not the same as the pressure computed at $Re_L = 0.42\times10^6$. This illustrates the paradox of the conical approximation applied to viscous flows: the calculations remain Reynolds-number dependent.

Test case No. 2

The grid used for the delta wing calculations is presented in Figure 2. It has 36 points along the surface and 50 across the shock layer, with $\beta = 1.05$. The numerical results are compared with the experimental data of Monnerie and Werlé (7). Those results were obtained with fourth-order damping coefficients equal to 0.4 in both η and ζ directions. Figure 9 shows a crosscut of the wing, the calculated shock shape and pressure contours, along with the experimental shock position in the plane of symmetry. The calculated surface pressure distribution is shown in Figure 10; since no data are available, it is compared with Prandtl Meyer expansion for the leeward and with inviscid cone theory for the windward. Figure 11 shows the Cartesian cross-flow velocity directions immediately above the wing (the scale in the normal direction is twice the scale in the tangential direction). The agreement with the experimental position of the main vortex is excellent. One can also see the small region of secondary separation near the tip. Pitot pressure measurements have also been performed in the region of the vortices. The pitot tube was parallel to the wing axis so that these measurements may be inaccurate, because of the large cross-flow velocities. In Figure 12, the data are compared with the computed pitot pressures based

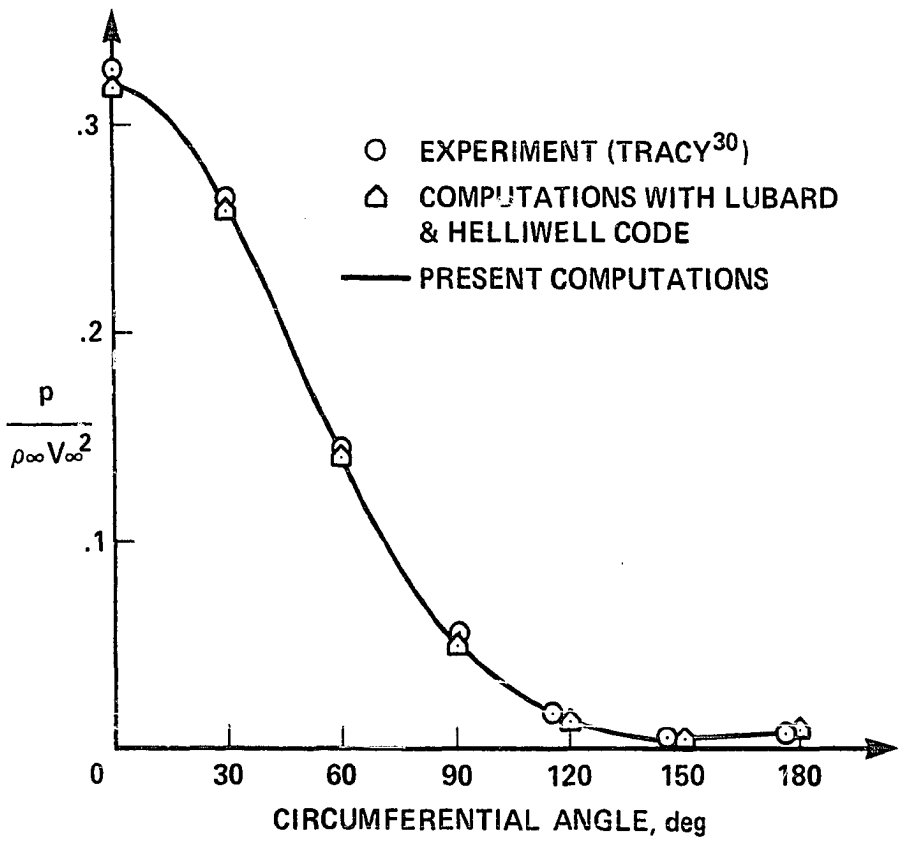

Figure 8. Test case No. 1 — conical approximation surface pressure

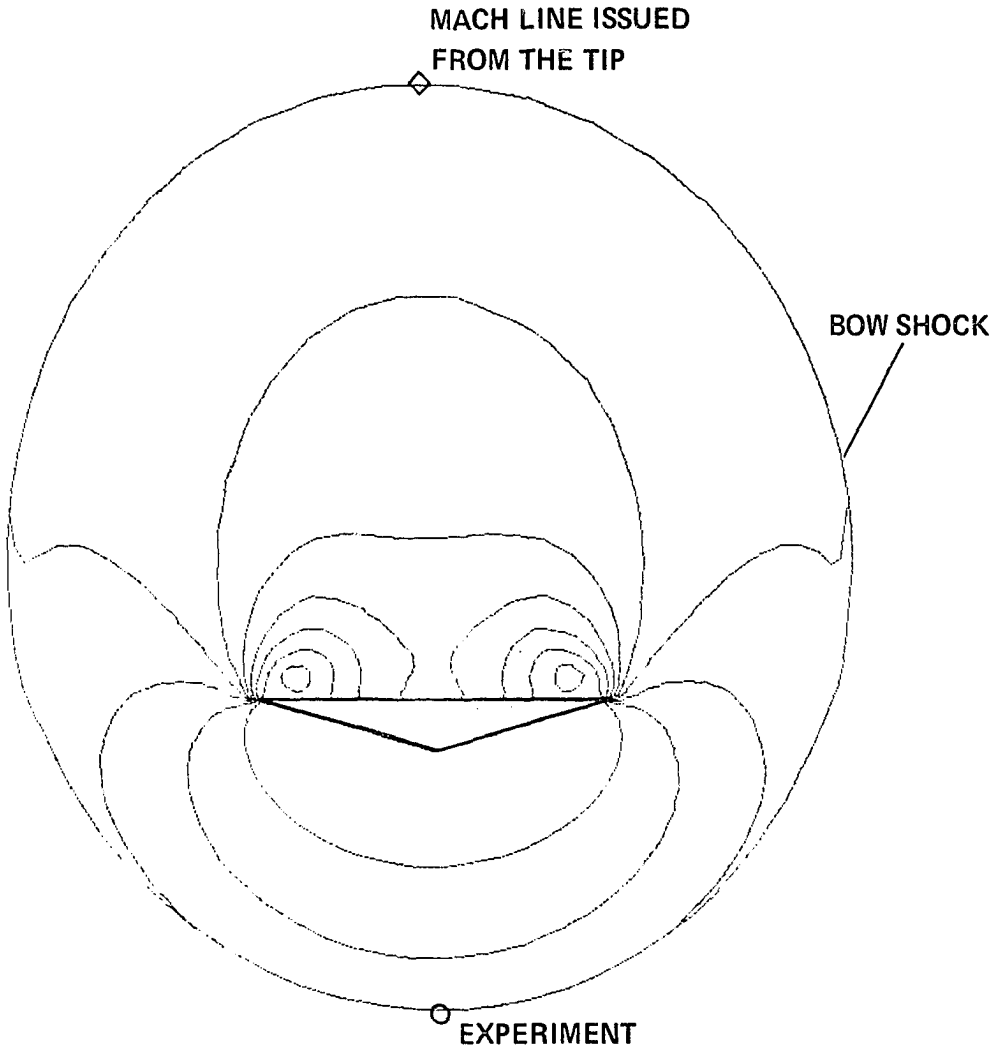

Figure 9. Test case No. 2 — conical approximation — pressure contours

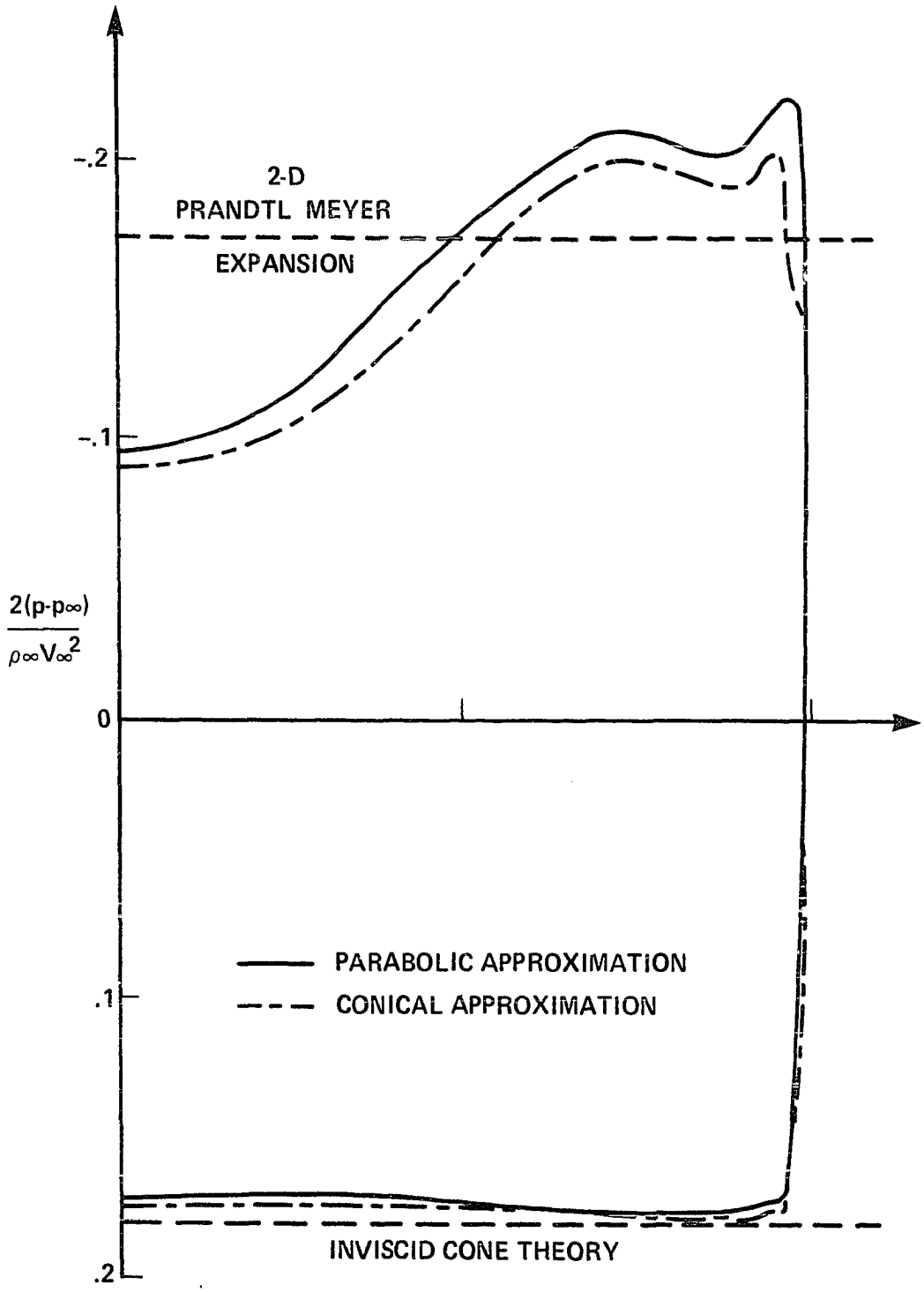

Figure 10. Test case No. 2 — surface pressure

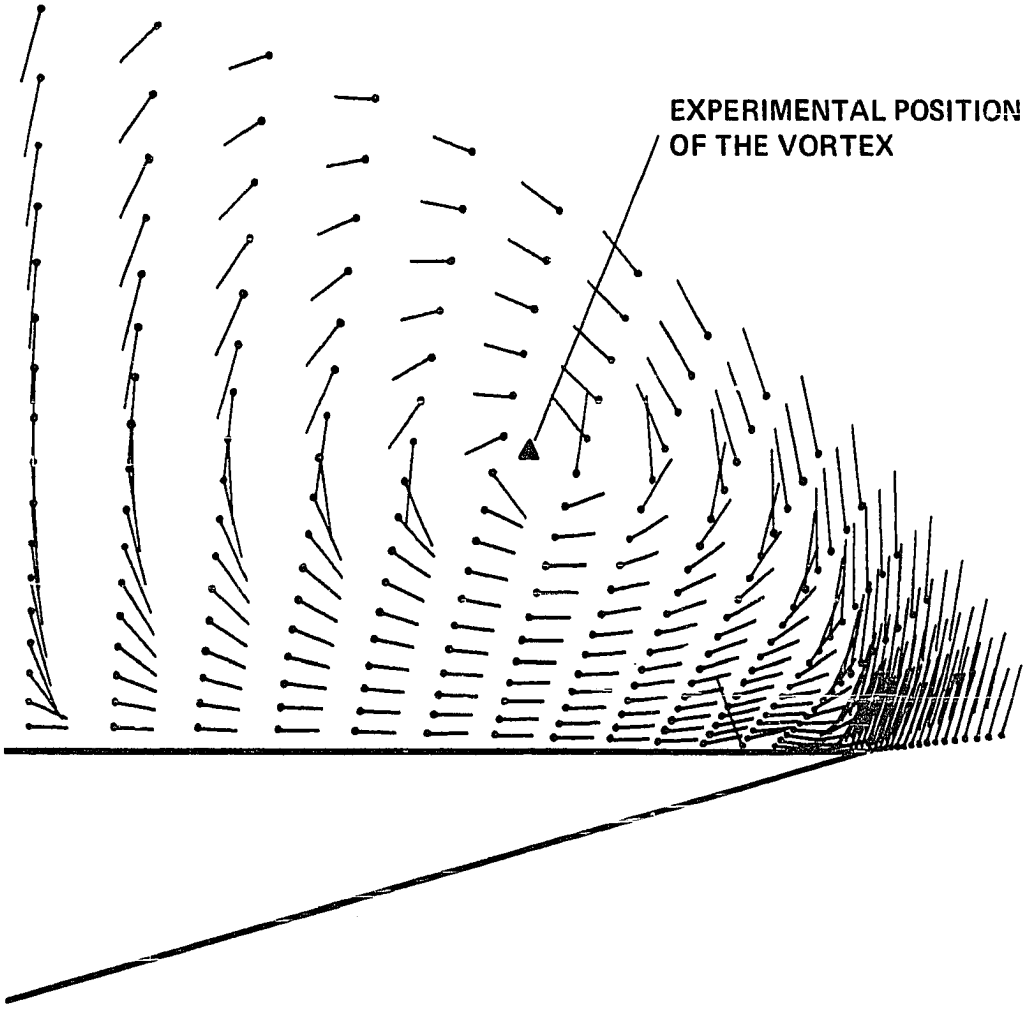

Figure 11. Test case No. 2 — conical approximation — cross-flow velocity directions

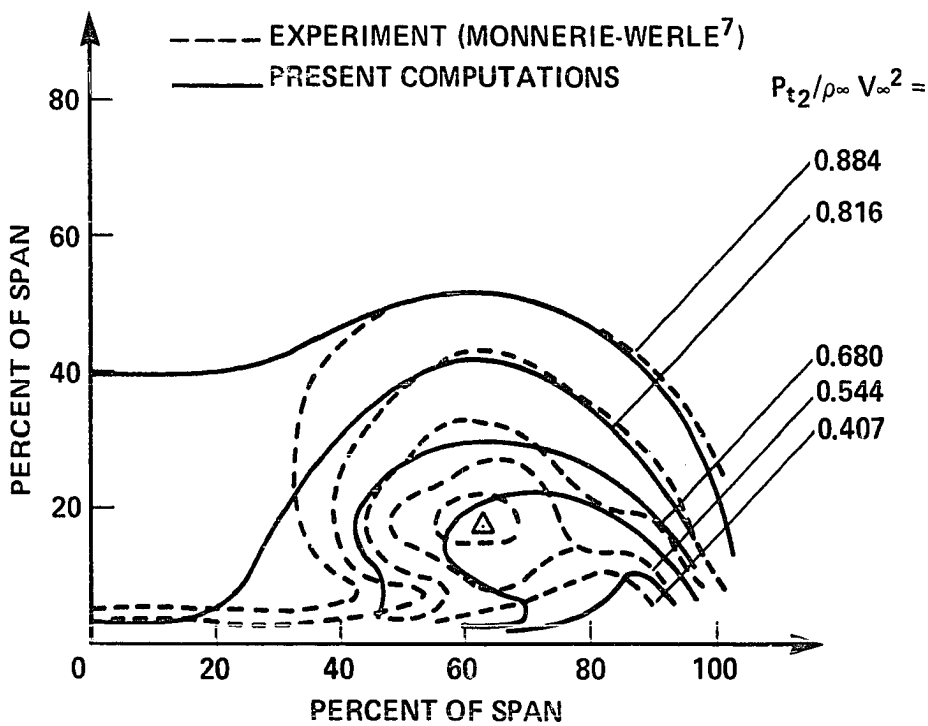

Figure 12. Test case No. 2 — conical approximation: pitot pressure contours

on the component of velocity parallel to the wing axis. As expected, the comparison is only approximative. Figure 13 shows the tangential velocities along a row of grid points immediately above the lee side of the wing and gives the location of the separation and reattachment of the secondary vortex. The disagreement with the experimental location is believed to be due to a relatively coarse computational grid used. However, in view of the relatively large Reynolds number, the comparisons may be complicated by the presence of turbulence in the experiment. The conical crossflow Mach number contours are given in Figure 14; only a small portion of the conical crossflow is supersonic. Figures 15 and 16 show the streamwise conical velocity and temperature profiles along three constant-ζ_1 rays emanating from the wing. Ray j = 1 is close to the windward plane of symmetry, Ray j = 30 goes through the main vortex, and Ray j = 36 is close to the leeward plane of symmetry. (A more exact definition of each of these rays is given in Table 2.) The inviscid portion of the flow field as well as the large viscous features (main vortex) are resolved properly. However, it should be noted that the numbers of grid points in the boundary layer (3 or 4) is not sufficient to give accurate shear stress and heat-transfer data at the wall.

Table 2. Geometric data for figures 15 and 16

Ray j=	1	30	36
y_B^a =	0.0685	0	0
z_B^a =	-.0123	.1336	-.01305
α =	-2.65°	150.88°	182.65°

[a] y_B and z_B are given in the plane x = 1.

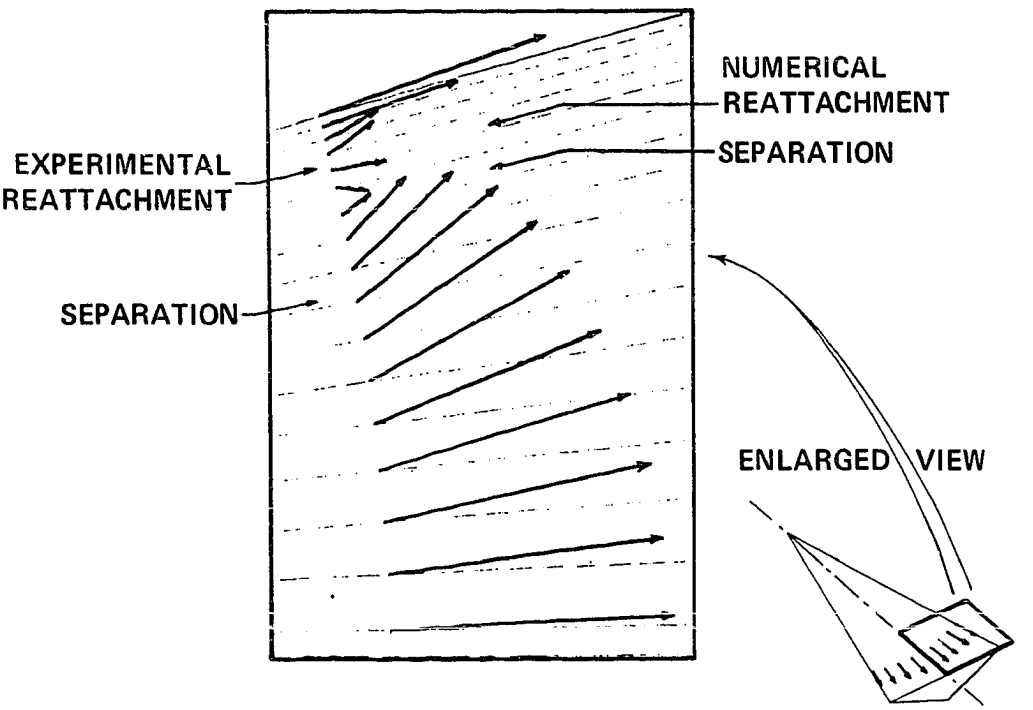

Figure 13. Test case No. 2 — conical approximation: calculated tangential velocities on upper surface

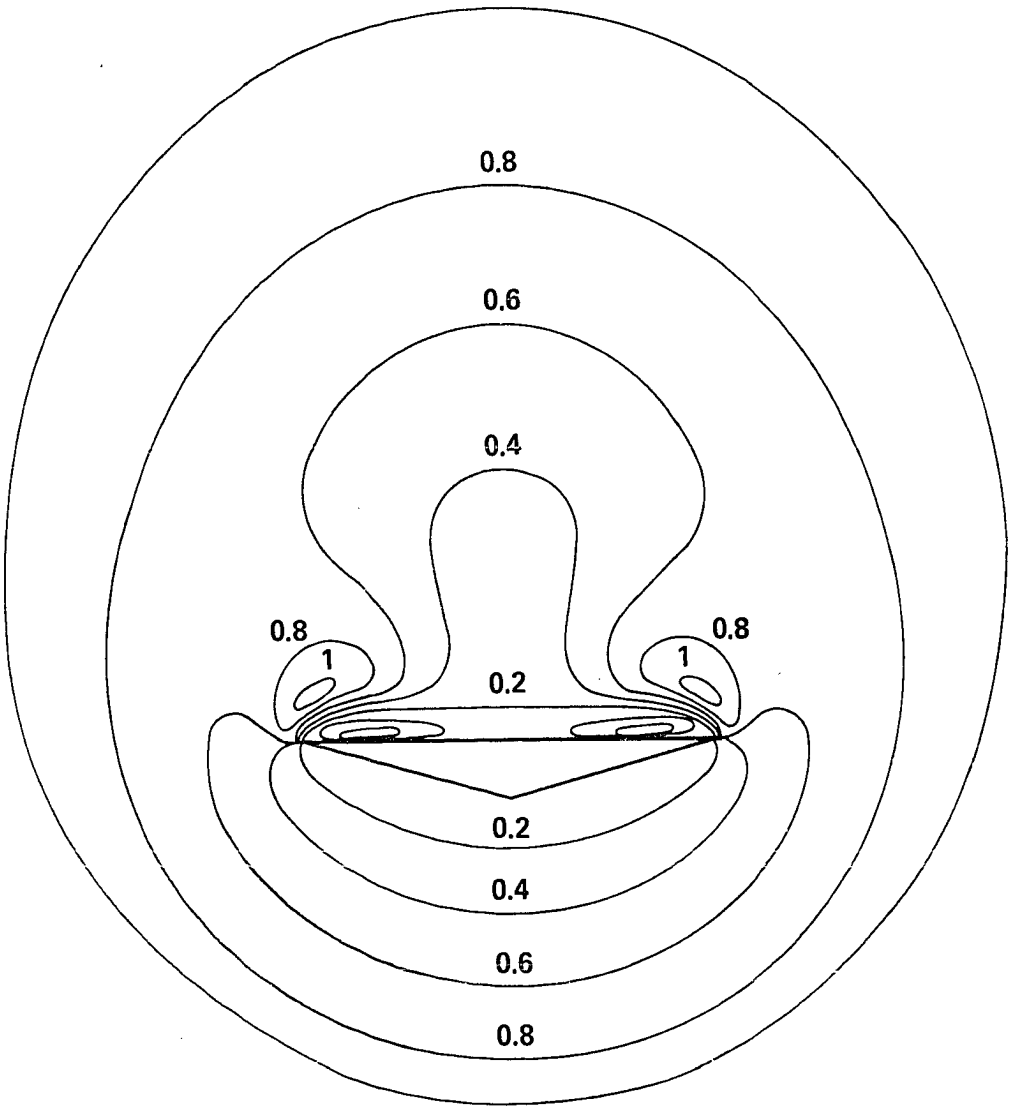

Figure 14. Test case No. 2 — conical approximation — conical crossflow Mach number

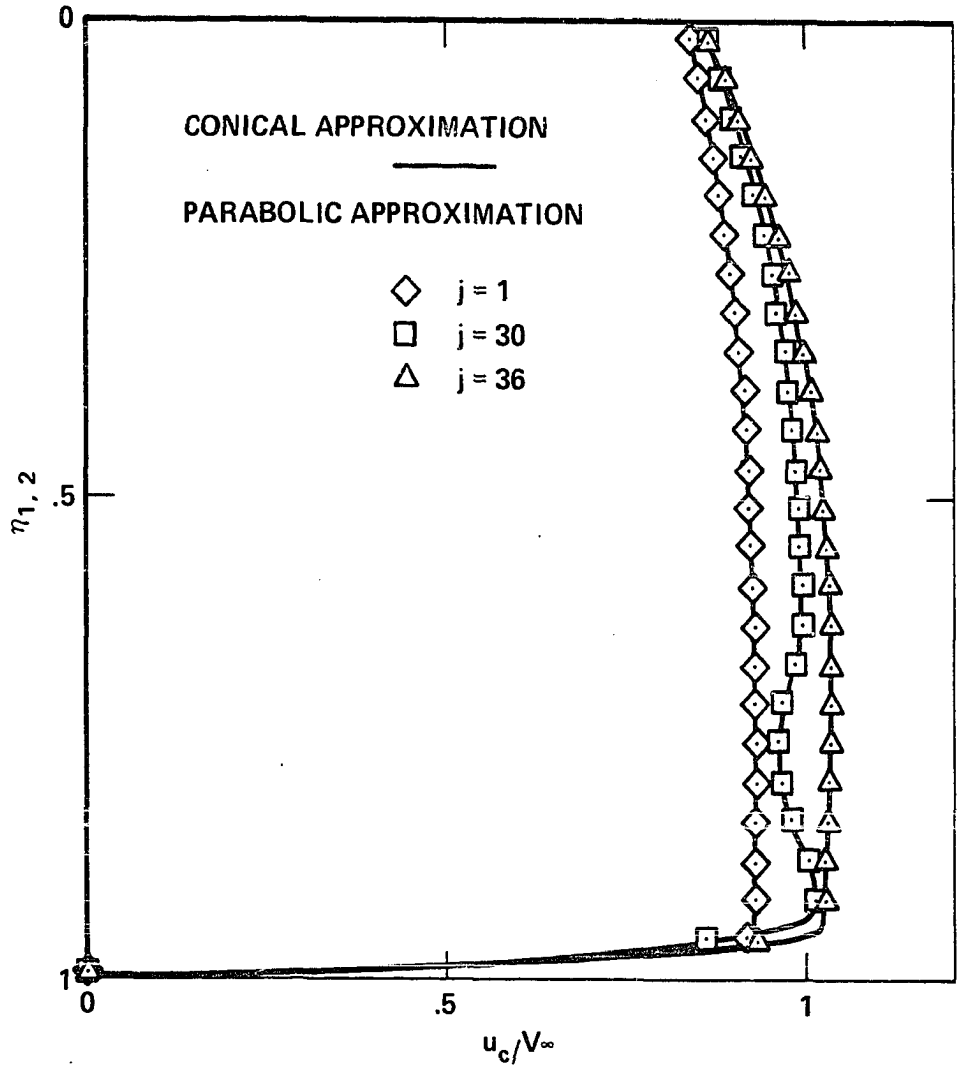

Figure 15. Test case No. 2 — comparison of streamwise conical velocity profiles

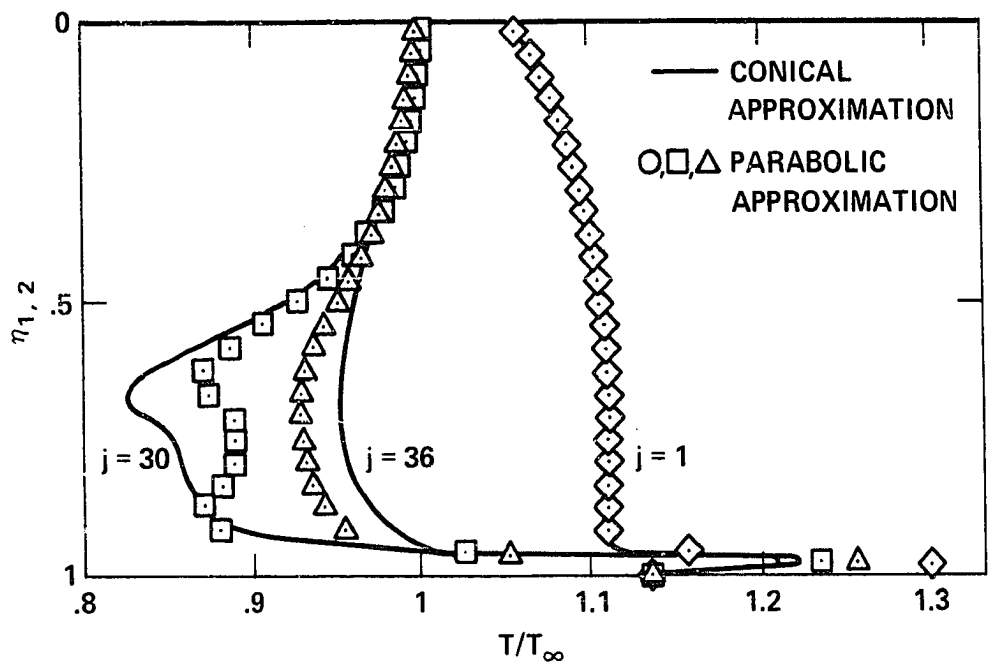

Figure 16. Test case No. 2 — comparison of temperature profiles

Test case No. 3

In this experiment by Thomann (8), measurements were made on half a delta wing placed on the side wall of the wind tunnel. For the computations, a grid similar to that of the previous case was used. The calculated and experimental surface pressure distributions are compared in Figure 17. Theory and experiment agree very well in the outboard portion of the wing but not in the center portion. This difference is believed to be caused by the wind-tunnel wall boundary layer (Figure 17) which extends over half the wing and is interacting with the flow around the wing.

Results for the Parabolic Approximation

Preliminary testing of the parabolic approximation was made by calculating the boundary-layer flow over a flat plate. The two-dimensional parabolized Navier-Stokes Equation 18 were solved using a simple Euler implicit finite-difference scheme. The conditions at the outer edge of the boundary layer were chosen as $M_\infty = 4$ and $Re_L = 1.9\times10^6$ where L is the length of the plate and the nondimensionalizing length. The wall temperature was taken as $T_w = T_\infty$ and the viscosity was kept constant. The calculations were started at station $x = 0.2$ (assuming a trapezoidal velocity profile) and advanced to station $x = 1$. The parameter $\omega(M_x)$ was evaluated by Equation 29 where the safety factor σ was set equal to 0.9. The term $\partial P/\partial x$ was approximated by a local backward difference. The results are compared with those of a standard boundary layer code (31). Figure 18 shows the streamwise velocity and temperature profiles. The agreement is very good and the slight differences in the region of higher temperature are believed to be due to the constant viscosity assumption.

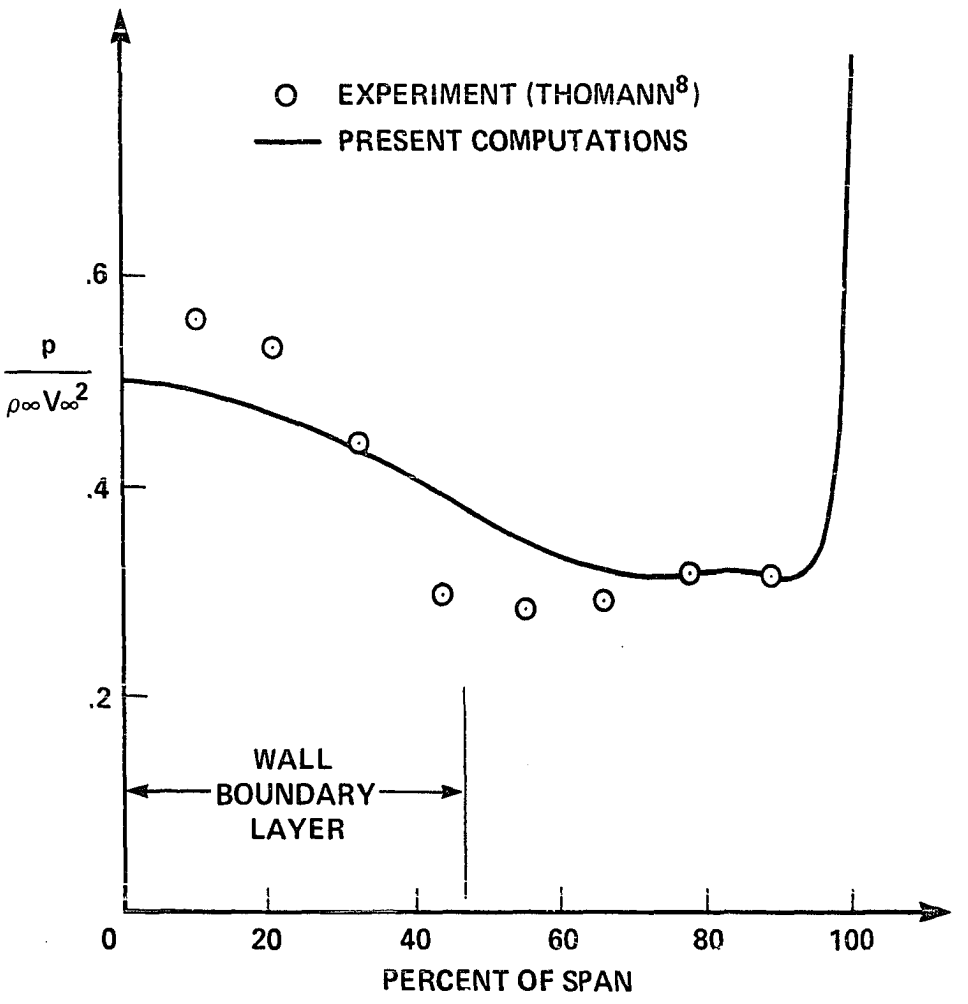

Figure 17. Test case No. 3 — conical approximation: pressure on upper surface

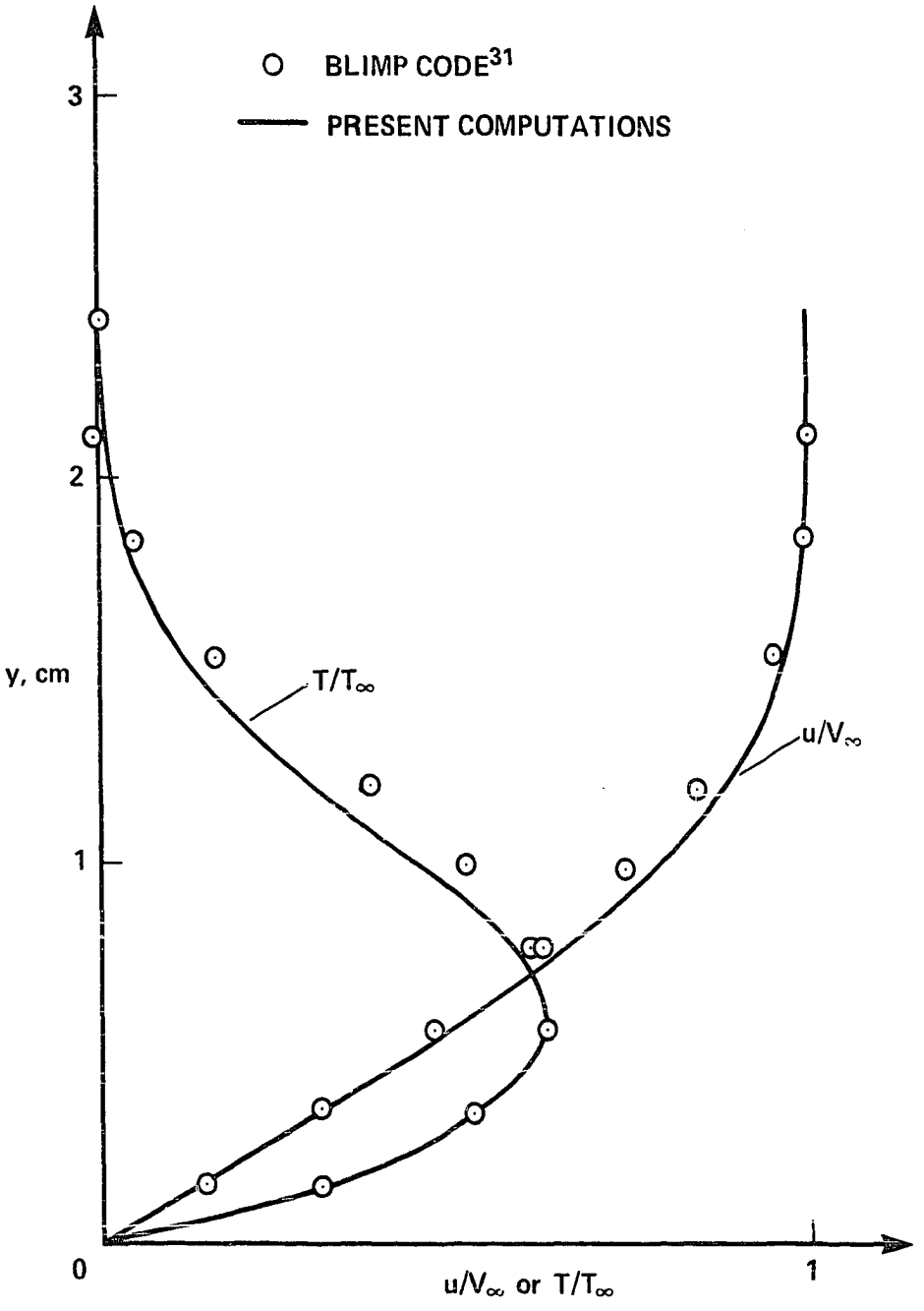

Figure 18. Parabolic approximation – boundary layer calculation

Test case No. 1

The full three-dimensional code described in Section III was then applied to the cone at angle of attack of test case No. 1. The finite-difference grid was identical to the one used for the conical calculations. The solution was marched from $\xi_2 = 0.2$ to $\xi_2 = 1$. Conical results at $\xi_2 = 0.2$ were taken as starting condition. Because the grid grows almost linearly with ξ_2, the step size $\Delta\xi_2$ was chosen proportional to ξ_2. The ratio $\Delta\xi_2/\xi_2 = 0.006$ was determined experimentally by requiring that the "shock fitting" procedure be stable. The smoothing constants ε_E and ε_I were such that $\varepsilon_E = 1.04\ \Delta\xi_2$ and $\varepsilon_I = 8.33\ \Delta\xi_2$. The parameter ω was calculated from Equation 29 with a safety factor of 0.8. The $\partial P_2/\partial\xi_2$ term was dropped from Equation 45. Figure 19 shows a crosscut of the cone and the bow shock, along with the tangential conical cross-flow velocity contours. The agreement with the experimental shock shape and separation point is again excellent. Also the velocity contours are almost identical to those obtained from the conical approximation (Figure 7). The surface pressure distribution is presented in Figure 20, and it compares very well with experiment and calculations performed with the Lubard and Helliwell code. Figure 21 shows the variation of the shear stress with ξ_2, in planes situated 5° off the plane of symmetry, on the leeward and windward of the cone. In logarithmic coordinates, they are compared with a straight line of slope (-1/2), which corresponds to the classic boundary-layer result. The deviation of the results from a straight line for the leeward may be due to the presence of cross flow. The short oscillation at the beginning of the calculations is a transient phenomenon caused by the approximate nature of the starting solution.

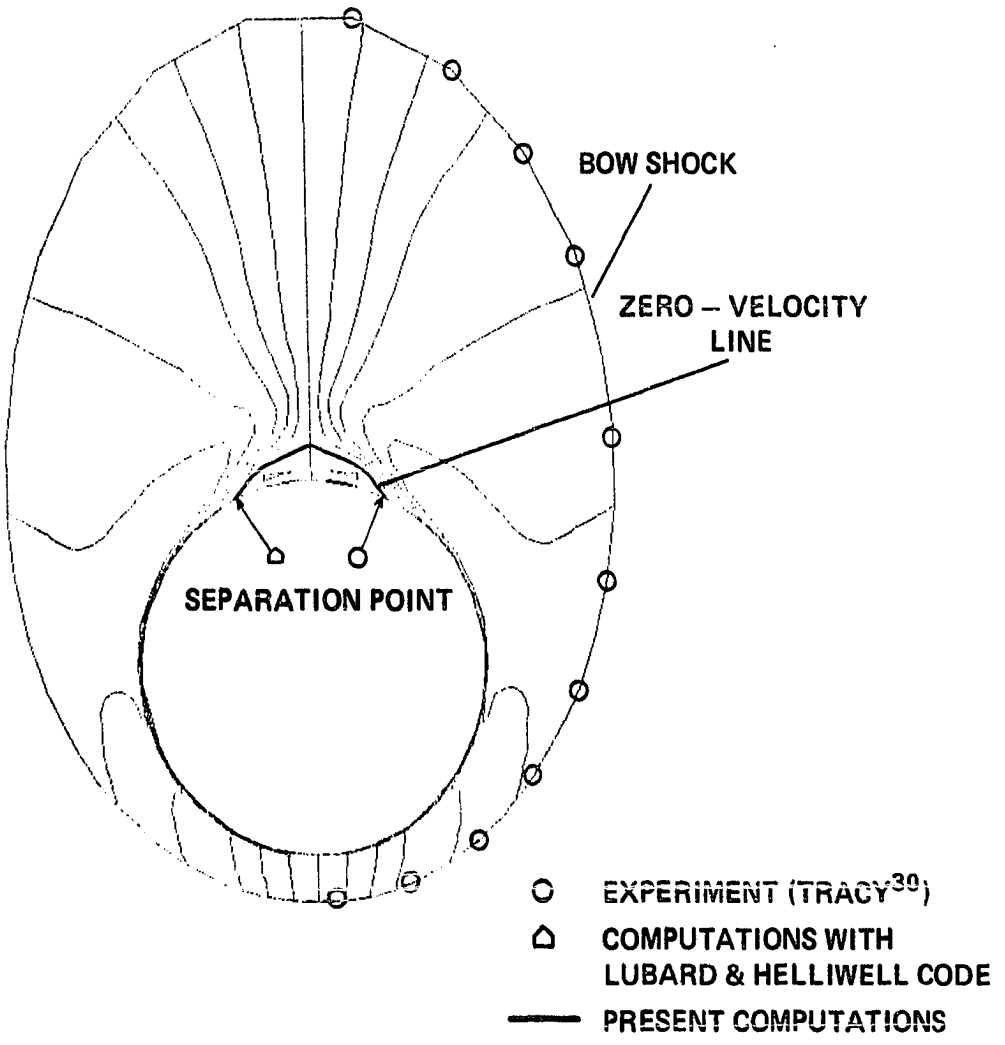

Figure 19. Test case No. 1 — parabolic approximation: cross-flow velocity contours.

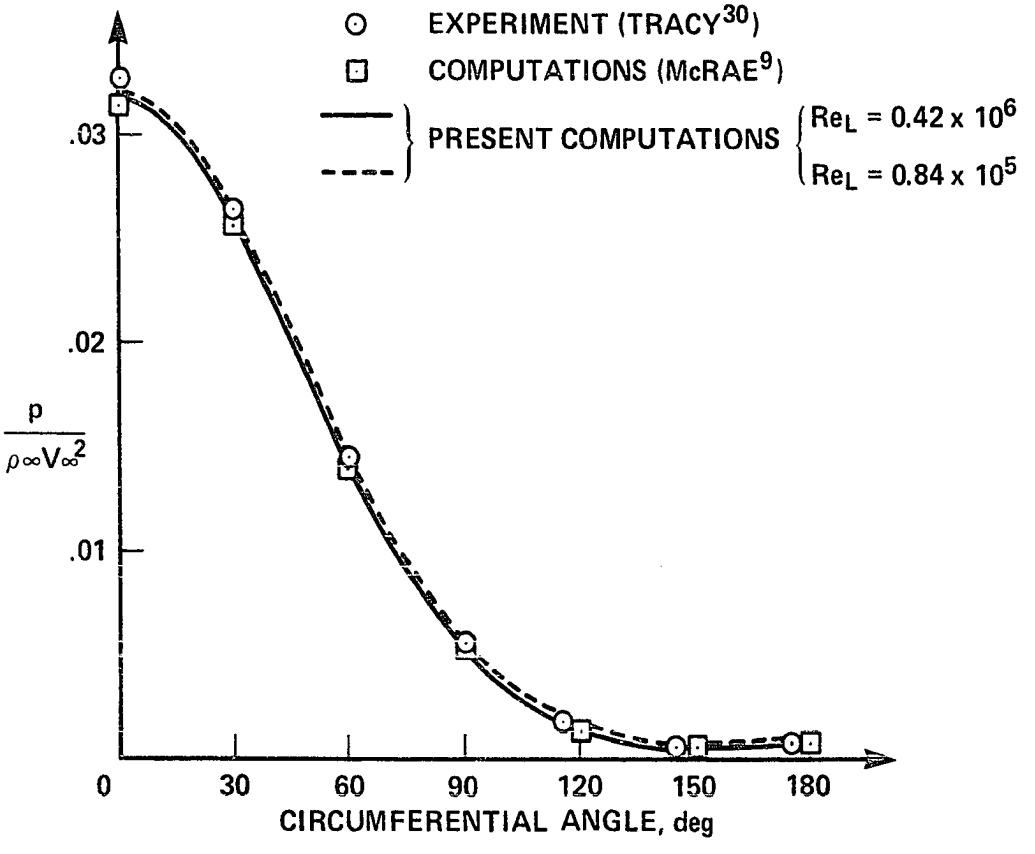

Figure 20. Test case No. 1 — parabolic approximation: surface pressure

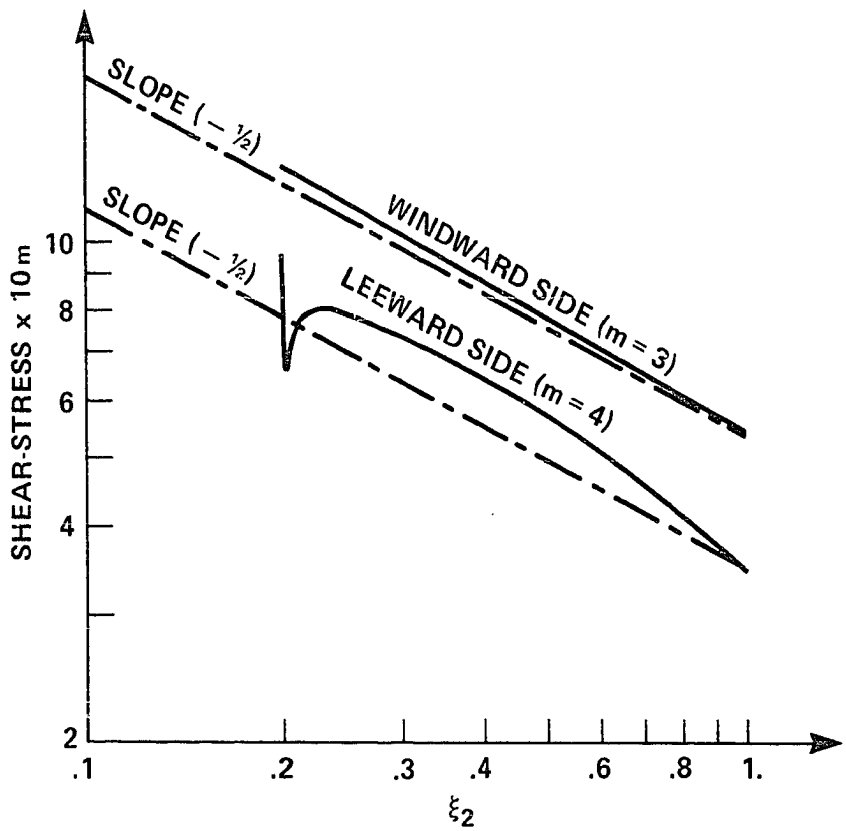

Figure 21. Test case No. 1 — parabolic approximation streamwise variation of the normal shear-stress

Some experimentation was done with the $\partial P_2/\partial \xi_2$ term. If approximated with a local backward difference it leads to quickly departing solutions. It was not possible to cure this problem by increasing the step size $\Delta \xi_2$ since this would have made the shock fitting procedure unstable. With the sublayer approximation, slowly oscillating or departing solutions were obtained for $1 < M_{x_e} < 2.5$. For $M_{x_e} > 2.5$ the results were within 5% of those obtained with $\partial P_2/\partial \xi_2 = 0$.

Test cast No. 2

For the delta wing, the solution was started from conical results at $\xi_2 = 0.5$ and advanced to $\xi_2 = 1$, with the same grid as in the conical calculations. Again the step size was allowed to grow linearly with ξ_2. However, in this case a more severe restriction on $\Delta \xi_2$ was necessary to prevent instabilities in the wing tip region so that $\Delta \xi_2 = 0.001\ \xi_2$. These results, apparently contradictory with the unconditional stability property of the implicit method, may be explained by the strong non-linearities in the vicinity of the tip. The smoothing coefficients were chosen so that $\varepsilon_E = 100 \cdot \Delta \xi_2$ (MacCormack smoothing) and $\varepsilon_I = 50\ \Delta \xi_2$. The parameter ω was computed from Equation 29 with $\sigma = 0.8$. The term $\partial P_2/\partial \xi_2$ was set equal to zero. The results are close to those obtained with the conical approximation. Figure 22 shows a crosscut of the wing and the bow shock, along with pressure contours. The surface pressure distribution is compared with the conical results in Figure 10. The curves are similar, differing only on the leeward by about 10-15%. Figure 23 shows the Cartesian cross-flow velocity directions just above the wing (the scale in the normal direction is twice that in the tangential direction). The position of the main vortex is predicted very well, but the region of

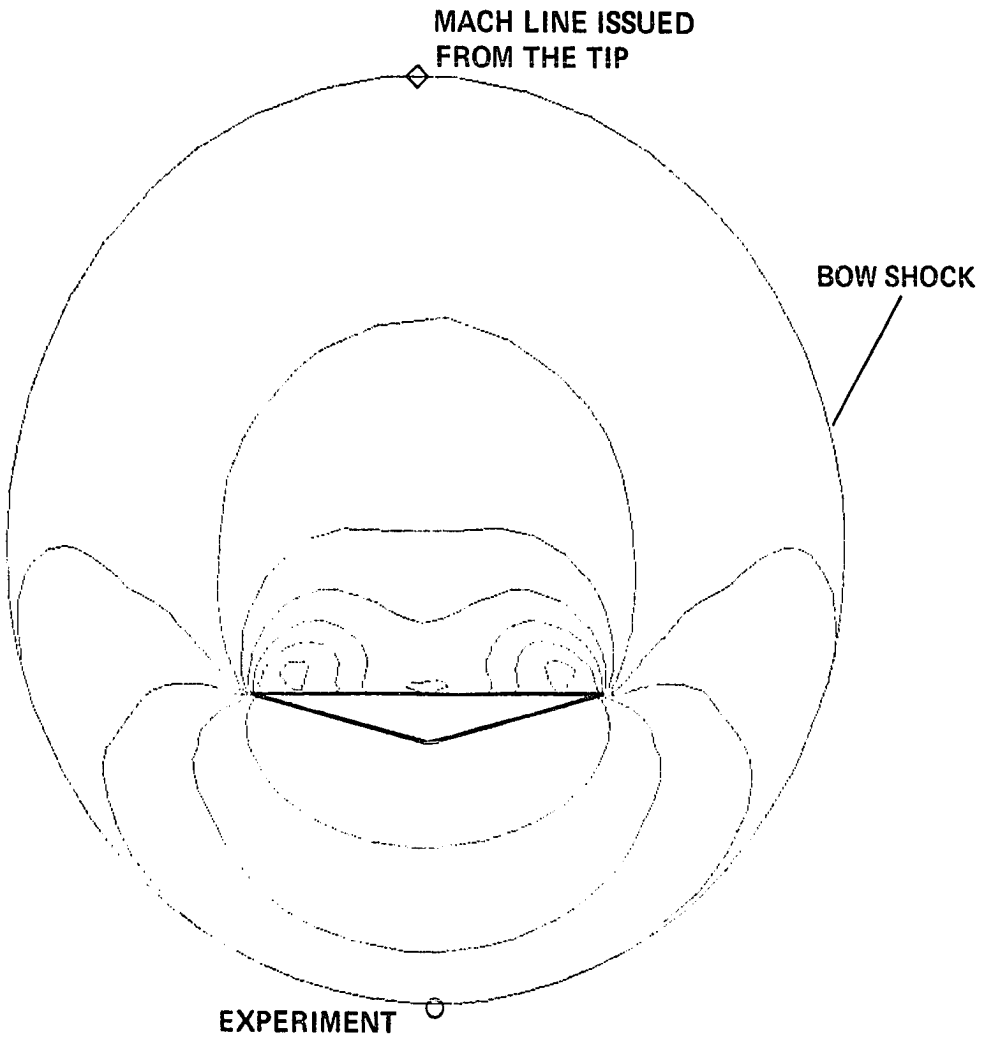

Figure 22. Test case No. 2 — parabolic approximation: pressure contours

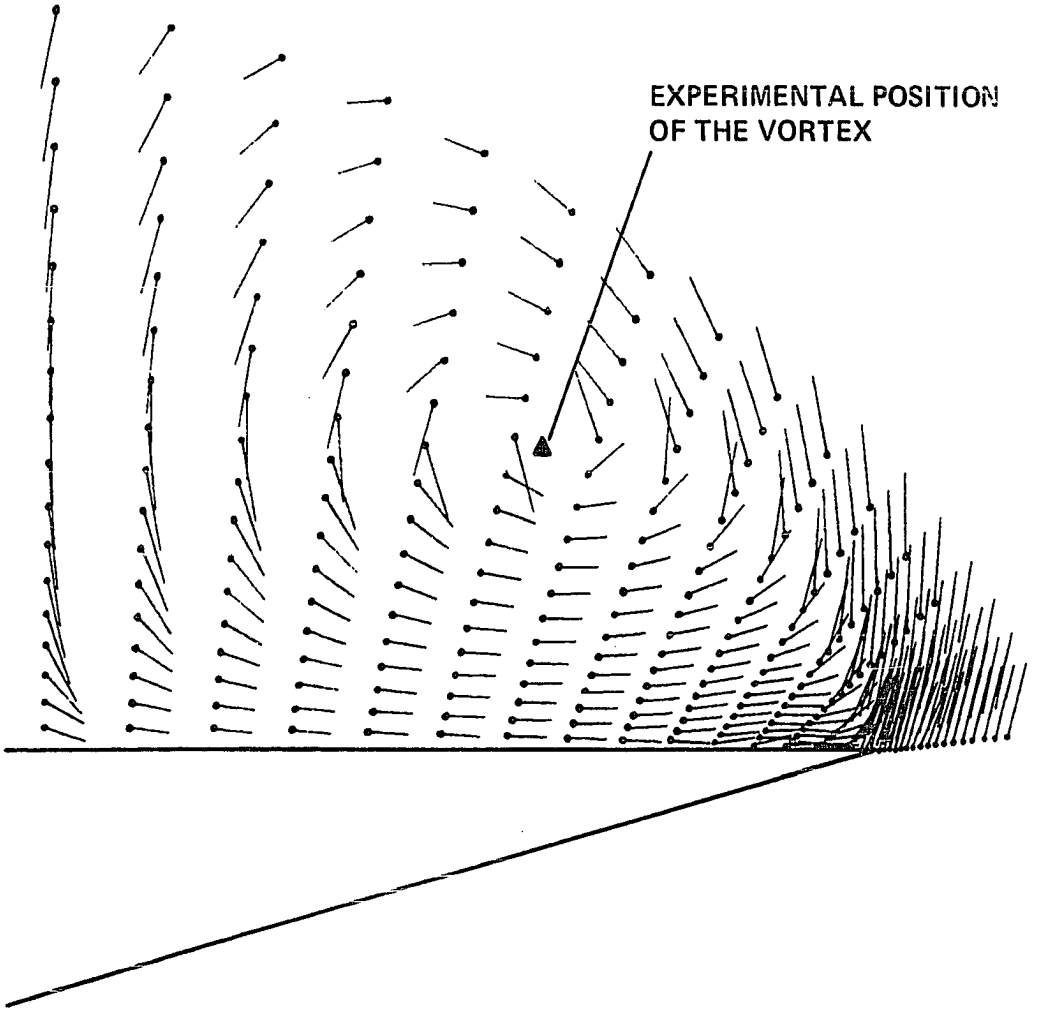

Figure 23. Test case No. 2 — parabolic approximation: cross-flow velocity directions

secondary separation is somewhat smaller; this might be due to excessive smoothing and lack of resolution. This lack of resolution is again brought out in Figures 15 and 16 where the streamwise conical velocity and temperature profiles along rays $j = 1$, $j = 30$, and $j = 36$ are compared with the conical results. The agreement for the velocity profiles is excellent. The temperature profiles on the windward also agree very well. Some disagreement appears on the leeward which is caused by the viscous terms not included in the conical approximation. The main differences however are in the boundary layer where the number of grid points is not sufficient for valid comparisons.

Computation Times

The results of this study were obtained on a CDC 7600 computer. The conical code required 3.61×10^{-4} sec of computer time per step and per grid point. About 15 min were needed to obtain a solution for the cone and close to 2 hr for the delta wing. These numbers could be improved upon by using some of the recently developed algorithms (32,26). However, the standard MacCormack scheme was chosen for its reliability and ease of programming and because the main point was to evaluate the conical approximation.

The parabolic code required 6.74×10^{-4} sec of computer time per step and per grid point. This is to be compared with an average of 54×10^{-4} sec for the Lubard and Helliwell code, thus providing a factor 8 improvement. The cone results took about 2 min of computer time and those for the delta wing less than 20 min.

CONCLUSIONS

In this study, typical realistic three-dimensional flows with large separated regions have been calculated in a reasonable amount of computer time. Both conical and parabolic approximations have predicted quantitatively the viscous and inviscid features of supersonic flows over cones and delta wings at angle of attack. Most notably determined is the location of the main vortex. The conical approach even produces results somewhat better than expected. However, the space-marching technique gives supplementary information about the streamwise variation of the flow variables and can be applied to nonconical bodies.

Also presented in this paper was a new approach for solving the parabolized Navier-Stokes equations. A procedure was developed to avoid upstream influence and still retain streamwise pressure variations. Also, a new implicit noniterative finite-difference algorithm was implemented which provides substantial improvement in computational efficiency over previous techniques. The results prove the approach to be justified. However, a new shock fitting procedure will be required to remove the step limitation of the present method. It will then be possible to include the source term $\partial P_2/\partial \xi_2$ (Equation 45) and thus retain the full pressure gradient p_{ξ_2}. Future work should also be directed toward calculating flow fields around nonconical bodies such as ogives and wing-body configurations.

REFERENCES

1. A. G. Parker. "Aerodynamic Characteristics of Slender Wings with Sharp Leading Edges — A Review," J. of Aircraft, 13, No. 3 (1976).

2. E. C. Polhamus. "Prediction of Vortex-Lift Characteristics by a Leading-Edge-Suction Analogy," J. of Aircraft, 8, No. 4 (1971).

3. R. T. Jones. "Properties of Low Aspect Ratio Pointed Wings at Speeds Above and Below the Speed of Sound," NACA Rept. 835, 1946.

4. K. W. Mangler and J. H. B. Smith. "Calculations of the Flow Past Slender Delta Wings with Leading Edge Separation," Royal Establishment, Farnborough, England, Rept. Aero. 2533, 1957.

5. J. A. Weber, G. W. Brune, F. T. Johnson, P. Lu, and P. E. Rubbert. "Three Dimensional Solution of Flows Over Wings with Leading Edge Vortex Separation," AIAA J., 14, No. 4 (1976).

6. A. P. Bazzhin. "Flat Slender Delta Wings in Supersonic Stream at Small Angles of Attack," Lecture Notes in Physics No. 35, Proceedings of the Fourth International Conference on Numerical Methods in Fluid Dynamics, 1971.

7. B. Monnerie and H. Werlé. "Etude de l'écoulement supersonique et hypersonique autour d'une aile élancée en incidence," AGARD CP-30, 1968.

8. H. Thomann. "Measurements of Heat Transfer, Recovery Temperature and Pressure Distribution on Delta Wings at M = 3," FAA Report 93, Sweden, 1962.

9. D. S. McRae. "A Numerical Study of Supersonic Viscous Cone Flow at High Angle of Attack," AIAA Paper 76-97, Washington, D.C., January 1976.

10. G. S. Bluford. "Navier-Stokes Solution of the Supersonic and Hypersonic Flow Field Around Planar Delta Wings," AIAA Paper 78-1136, Seattle, Wash., 1978.

11. H. K. Cheng, S. Y. Chen, R. Mobley, and C. R. Huber. "The Viscous Hypersonic Slender-Body Problem: A Numerical Approach Based on a System of Composite Equations," RM 6193-PR, The Rand Corp., Santa Monica, Calif., May 1970.

12. S. G. Rubin and T. C. Lin. "Numerical Methods for Two- and Three-Dimensional Viscous Flow Problems: Application to Hypersonic Leading Edge Equations." PIBAL Rept. No. 71-8, Polytechnic Institute of Brooklyn, Farmingdale, N.Y., April 1971.

13. S. C. Lubard and W. S. Helliwell. "Calculation of the Flow on a Cone at High Angle of Attack," RDA TR 150, R&D Associates, Santa Monica, Calif., Feb. 1973.

14. H. Viviand. "Conservative Forms of Gas Dynamic Equations," La Recherche Aérospatiale, No. 1, Jan.-Feb. 1974.

15. G. O. Roberts. Computational Meshes for Boundary Layer Problems, Lecture Notes in Physics, Springer-Verlag, New York, 1971.

16. A. Lerat and J. Sides. "Numerical Calculation of Unsteady Transonic Flows," AGARD Meeting of Unsteady Airloads in Separated and Transonic Flow, Lisbon, April 1977.

17. J. L. Steger. "Implicit Finite-Difference Simulation of Flow About Arbitrary Geometries with Application to Airfoils," AIAA Paper 77-665, Albuquerque, N. Mex., June 1977.

18. R. W. MacCormack. "The Effect of Viscosity in Hypervelocity Impact Cratering," AIAA Paper 69-354, Cincinnati, Ohio, 1969.

19. J. C. Tannehill, T. L. Holst and J. V. Rakich. "Numerical Computation of Two-Dimensional Viscous Blunt Body Flows with an Impinging Shock," AIAA J., 4, No. 2 (1976).

20. R. W. MacCormack and B. S. Baldwin. "A Numerical Method for Solving the Navier-Stokes Equations with Application to Shock Boundary Layer Interactions," AIAA Paper 75-1, Pasadena, Calif. 1975.

21. M. J. Lighthill. "On Boundary Layers and Upstream Influence. II. Supersonic Flows Without Separation," Proc. Roy. Soc. A., 217, 1953.

22. Lindemuth, I. and Killeen, I., "Alternating Direction Implicit Techniques for Two Dimensional Magnetohydrodynamics Calculations," J. of Comput. Phys., 13, (1973).

23. W. R. Briley and H. McDonald. "Three-Dimensional Supersonic Flow of a Viscous or Inviscid Flow," J. of Comput. Phys., 19 (1975).

24. W. R. Briley and H. McDonald. "Solution of the Multidimensional Compressible Navier-Stokes Equations by a Generalized Implicit Method," J. of Comput. Phys., 24 (1977).

25. R. Beam and R. F. Warming. "An Implicit Finite-Difference Algorithm for Hyperbolic Systems in Conservation-Law-Form," J. of Comput. Phys., 22 (1976).

26. R. Beam and R. F. Warming. "An Implicit Factored Scheme for the Compressible Navier-Stokes Equations," AIAA Paper 77-645, Albuquerque, N. Mex., June 1977.

27. R. F. Warming and R. Beam. "On the Construction and Application of Implicit Factored Schemes for Conservation Laws," SIAM-AMS Proceedings of the Symposium on Computational Fluid Dynamics, New York, April 1977.

28. J. A. Desideri, J. L. Steger and J. C. Tannehill. "Improving the Steady State Convergence of Implicit Finite-Difference Algorithms for the Euler Equations" (to be published).

29. P. D. Thomas, M. Vinokur, R. A. Bastianon and R. J. Conti. "Numerical Solution for Three-Dimensional Inviscid Supersonic Flows," AIAA J., 10, No. 7 (1972).

30. R. R. Tracy. "Hypersonic Flow Over a Yawed Circular Cone," Ph.D. Thesis, California Institute of Technology, Graduate Aeronautical Labs, Firestone Flight Sciences Lab., August 1963.

31. H. Tong. "Nonequilibrium Chemistry Boundary Layer Integral Matrix Procedure, User's Manual Parts I and II." Aerotherm Corp. Rept. UM-73-37, April 1973.

32. R. W. MacCormack. "An Efficient Method for Solving the Time Dependent Compressible Navier-Stokes Equation at High Reynolds Number," NASA TM X-73,129, July 1976.

ACKNOWLEDGMENTS

The author wishes to express his most sincere gratitude to Mr. J. V. Rakich for his guidance and suggestions and, most of all, for his friendship; to Dr. J. C. Tannehill for his support throughout this work; and to all the people of the Experimental Fluid Dynamics Branch. The author is also thankful to Mrs. June Zyskowski for her patience and skill in putting together this manuscript.

This work was supported by NASA Ames Research Center under Grant NGR 16-002-038 and the Engineering Research Institute, Iowa State University, Ames, Iowa.

APPENDIX A: GOVERNING EQUATIONS

The fundamental equations governing the unsteady flow of a perfect gas, without body forces or external heat additions, can be written in conservation-law form for a Cartesian coordinate system as

$$\frac{\partial U}{\partial t} + \frac{\partial (E - E_v)}{\partial x} + \frac{\partial (F - F_v)}{\partial y} + \frac{\partial (G - G_v)}{\partial z} = 0$$

where

$$U = \begin{bmatrix} \rho \\ \rho u \\ \rho v \\ \rho w \\ \rho e_t \end{bmatrix} \qquad e_t = e + \frac{u^2 + v^2 + w^2}{2}$$

$$E = \begin{bmatrix} \rho u \\ \rho u^2 + p \\ \rho uv \\ \rho uw \\ (\rho e_t + p)u \end{bmatrix} \qquad E_V = \begin{bmatrix} 0 \\ \sigma_{xx} \\ \tau_{xy} \\ \tau_{xz} \\ u\sigma_{xx} + v\tau_{xy} + w\tau_{xz} + q_x \end{bmatrix}$$

$$F = \begin{bmatrix} \rho v \\ \rho uv \\ \rho v^2 + p \\ \rho vw \\ (\rho e_t + p)v \end{bmatrix} \qquad F_V = \begin{bmatrix} 0 \\ \tau_{xy} \\ \sigma_{yy} \\ \tau_{yz} \\ u\tau_{xy} + v\sigma_{yy} + w\tau_{yz} + q_y \end{bmatrix}$$

$$G = \begin{bmatrix} \rho w \\ \rho uw \\ \rho vw \\ \rho w^2 + p \\ (\rho e_t + p)w \end{bmatrix} \qquad G_V = \begin{bmatrix} 0 \\ \tau_{xz} \\ \tau_{yz} \\ \sigma_{zz} \\ u\tau_{xz} + v\tau_{yz} + w\sigma_{zz} + q_z \end{bmatrix}$$

In addition, an equation of state must be specified. For a perfect gas, it can be written as

$$p = (\gamma - 1)\rho e$$

The Navier-Stokes expressions for the components of the shearing stress tensor and the heat-flux vector are

$$\sigma_{xx} = \frac{2\mu}{Re}\left(\frac{\partial u}{\partial x} - \frac{1}{3}\,\mathrm{div}\,\vec{V}\right)$$

$$\sigma_{yy} = \frac{2\mu}{Re}\left(\frac{\partial v}{\partial y} - \frac{1}{3}\,\mathrm{div}\,\vec{V}\right)$$

$$\sigma_{zz} = \frac{2\mu}{Re}\left(\frac{\partial w}{\partial z} - \frac{1}{3}\,\mathrm{div}\,\vec{V}\right)$$

$$\tau_{xy} = \frac{\mu}{Re}\left(\frac{\partial u}{\partial y} + \frac{\partial v}{\partial x}\right)$$

$$\tau_{xz} = \frac{\mu}{Re}\left(\frac{\partial u}{\partial z} + \frac{\partial w}{\partial x}\right)$$

$$\tau_{yz} = \frac{\mu}{Re}\left(\frac{\partial v}{\partial z} + \frac{\partial w}{\partial y}\right)$$

$$q_x = \frac{\mu}{(\gamma - 1)M_\infty^2 Re_L Pr}\frac{\partial T}{\partial x}$$

$$q_y = \frac{\mu}{(\gamma - 1)M_\infty^2 Re_L Pr}\frac{\partial T}{\partial y}$$

$$q_z = \frac{\mu}{(\gamma - 1)M_\infty^2 Re_L Pr}\frac{\partial T}{\partial z}$$

where the coefficient of molecular viscosity μ is obtained from Sutherland's equation and the coefficient of thermal conductivity is computed by assuming a constant Prandtl number $Pr = 0.72$.

These equations have been nondimensionalized as follows (the bars denote the dimensional quantities)

$$x = \frac{\bar{x}}{L} \qquad y = \frac{\bar{y}}{L} \qquad z = \frac{\bar{z}}{L} \qquad t = \frac{\bar{t}}{L/V_\infty}$$

$$u = \frac{\bar{u}}{V_\infty} \qquad v = \frac{\bar{v}}{V_\infty} \qquad w = \frac{\bar{w}}{V_\infty}$$

$$\rho = \frac{\bar{\rho}}{\rho_\infty} \qquad p = \frac{\bar{p}}{\rho_\infty V_\infty^2} \qquad T = \frac{\bar{T}}{T_\infty} \qquad e = \frac{\bar{e}}{V_\infty^2}$$

$$\mu = \frac{\bar{\mu}}{\mu_\infty}$$

where L is the length defined by the Reynolds number

$$Re_L = \frac{\rho_\infty V_\infty L}{\mu_\infty}$$

APPENDIX B: "SHOCK-FITTING" PROCEDURES

Conical Approximation

The conical shock is allowed to move toward its steady-state position. The displacement of the shock is introduced through the time dependence of the shock standoff distance δ in the plane $x = 1$. The problem is to express δ_t as a function of the fluid velocity at infinity and the relative fluid velocity normal to the shock (see Figure 24).

The local velocity of the shock is given by

$$\vec{U}_s = -\delta_t \vec{n} \cdot \vec{N}_s \tag{B1}$$

where $\vec{N}_s$ denotes the inward unit normal to the shock

$$\vec{N}_s = \left. \frac{\left(y \frac{\partial z}{\partial \zeta_1} - z \frac{\partial y}{\partial \zeta_1}\right)\vec{i} - \frac{\partial z}{\partial \zeta_1}\vec{j} + \frac{\partial y}{\partial \zeta_1}\vec{k}}{\sqrt{\left(y \frac{\partial z}{\partial \zeta_1} - z \frac{\partial y}{\partial \zeta_1}\right)^2 + \left(\frac{\partial y}{\partial \zeta_1}\right)^2 + \left(\frac{\partial z}{\partial \zeta_1}\right)^2}} \right|_{\text{shock}} \tag{B2}$$

and the subscript shock refers to values along the shock in the plane $x = 1$. The algebraic value of the local shock velocity can be related to δ_t by

$$U_s = \left. \frac{\delta_t\left(\frac{\partial z}{\partial \zeta_1} \cos\alpha - \frac{\partial y}{\partial \zeta_1} \sin\alpha\right)}{\sqrt{\left(y \frac{\partial z}{\partial \zeta_1} - z \frac{\partial y}{\partial \zeta_1}\right)^2 + \left(\frac{\partial y}{\partial \zeta_1}\right)^2 + \left(\frac{\partial z}{\partial \zeta_1}\right)^2}} \right|_{\text{shock}} \tag{B3}$$

The vector component of the fluid velocity normal to and measured with respect to the moving shock is

$$V_1 = (\vec{V}_\infty + U_s \vec{N}_s) \cdot \vec{N}_s \tag{B4}$$

Substituting for $\vec{V}_\infty$, U_s, and $\vec{N}_s$, δ_t can be obtained as

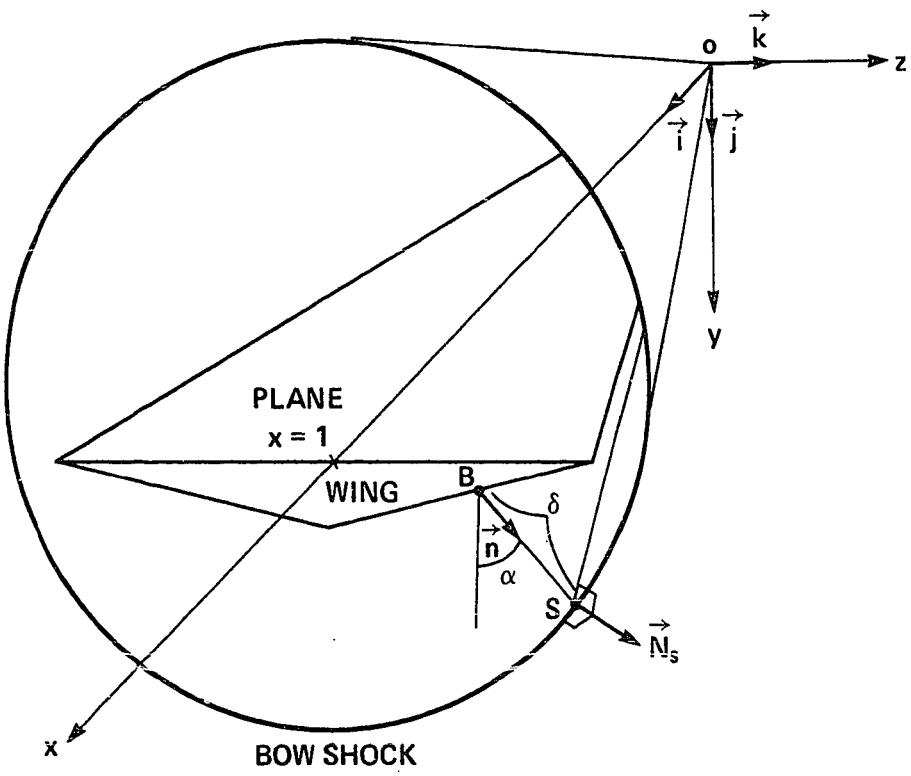

Figure 24. Shock fitting notations

$$\delta_t = \left.\frac{\left[V_1\sqrt{\left(y\frac{\partial z}{\partial \zeta_1} - z\frac{\partial y}{\partial \zeta_1}\right)^2 + \left(\frac{\partial y}{\partial \zeta_1}\right)^2 + \left(\frac{\partial z}{\partial \zeta_1}\right)^2} - \left(y\frac{\partial z}{\partial \zeta_1} - z\frac{\partial y}{\partial \zeta_1}\right)u_\infty + \frac{\partial z}{\partial \zeta_1}v_\infty - \frac{\partial y}{\partial \zeta_1}w_\infty\right]}{\frac{\partial z}{\partial \zeta_1}\cos\alpha - \frac{\partial y}{\partial \zeta_1}\sin\alpha}\right|_{\text{shock}} \tag{B5}$$

Finally, the metric coefficient $\partial\eta_1/\partial t$ results from the differentiation of the stretching function (11c)

$$\frac{\partial \eta_1}{\partial t} = \frac{2\beta}{\left[\beta^2 - \left(\frac{\delta - s}{\delta}\right)^2\right]\mathrm{Ln}\left(\frac{\beta+1}{\beta-1}\right)}\frac{s}{\delta^2}\delta_t \tag{B6}$$

where s is given by Equation 11c. From this point on, the method is identical to that described in Reference 19.

Parabolic Approximation

As the calculations proceed downstream, the position of the shock is computed simultaneously with the rest of the solution. The shock standoff distance δ is obtained from the values at ξ_2 through an Euler integration

$$\delta(\xi_2 + \Delta\xi_2) = \delta(\xi_2) + \frac{\partial \delta}{\partial \xi_2}\Delta\xi_2 \tag{B7}$$

The problem is to determine the slope δ_{ξ_2} at station ξ_2. The inward unit normal to the shock is given by

$$N_s = \frac{\ell\vec{i} - \frac{\partial z}{\partial \zeta_2}\vec{j} + \frac{\partial y}{\partial \zeta_2}\vec{k}}{\sqrt{\ell^2 + \left(\frac{\partial y}{\partial \zeta_2}\right)^2 + \left(\frac{\partial z}{\partial \zeta_2}\right)^2}} \tag{B8}$$

where

$$\ell = \delta_{\xi_2}\left(\frac{\partial z}{\partial \zeta_2}\cos\alpha - \frac{\partial y}{\partial \zeta_2}\sin\alpha\right) + \left(\frac{\partial z}{\partial \zeta_2} b_{2_B} - \frac{\partial y}{\partial \zeta_2} c_{2_B}\right) \tag{B9}$$

and the derivatives with respect to ζ_2 are taken along the shock. If V_1 denotes the upstream flow velocity normal to the shock

$$V_1^2 = (\vec{N}_S \cdot \vec{V}_\infty)^2 \tag{B10}$$

Substituting for $\vec{V}_\infty$ and $\vec{N}_S$, this equation can be solved for δ_{ξ_2} (the root such that $\delta_{\xi_2} > 0$ is retained)

$$\delta_{\xi_2} = \frac{\left\{\begin{array}{l} u_\infty\left(\frac{\partial z}{\partial \zeta_2} v_\infty - \frac{\partial y}{\partial \zeta_2} w_\infty\right) \\ + V_1(u_\infty^2 - v_1^2) \\ \left[\left(\frac{\partial y}{\partial \zeta_2}\right)^2 + \left(\frac{\partial z}{\partial \zeta_2}\right)^2\right] \\ + \left(\frac{\partial z}{\partial \zeta_2} v_\infty - \frac{\partial y}{\partial \zeta_2} w_\infty\right)^2 \end{array}\right\}}{u_\infty^2 - v_\infty^2} - \left(\frac{\partial z}{\partial \zeta_2} b_{2_B} - \frac{\partial y}{\partial \zeta_2} c_{2_B}\right)}{\frac{\partial z}{\partial \zeta_2}\cos\alpha - \frac{\partial y}{\partial \zeta_2}\sin\alpha} \tag{B11}$$

The metric coefficient $\partial\eta_2/\partial a_2$ is obtained by differentiating Equation 11c:

$$\frac{\partial \eta_2}{\partial a_2} = \frac{2\beta}{\left\{\beta^2 - \left(\frac{\delta - s}{\delta}\right)^2\right\}\mathrm{Ln}\left(\frac{\beta+1}{\beta-1}\right)} \cdot \frac{s}{\delta^2} \cdot \left(\delta_{\xi_2} - \frac{\delta}{\xi_2}\right) \tag{B12}$$

where s is given by Equation 11c. Once the new shock position is determined, the application of a one-sided version of the finite-difference algorithm gives the pressure behind the shock. The rest of the flow variables result from the exact shock jump relations.

APPENDIX C: JACOBIANS $\partial F_2/\partial U_2$, $\partial G_2/\partial U_2$, and $\partial E_2^*/\partial U_2$

The Jacobians $\partial F_2/\partial U_2$ and $\partial G_2/\partial U_2$ are given by

$$\frac{\partial F_2}{\partial U_2} = \frac{\partial}{\partial U_2}\left\{\frac{a_2}{\mathscr{D}_2}\left[\left(a_2\frac{\partial \eta_2}{\partial a_2} - b_2\frac{\partial \eta_2}{\partial b_2} - c_2\frac{\partial \eta_2}{\partial c_2}\right)(E - E_v) + \frac{\partial \eta_2}{\partial b_2}(F - F_v) + \frac{\partial \eta_2}{\partial c_2}(G - G_v)\right]\right\} \tag{C1}$$

$$\frac{\partial G_2}{\partial U_2} = \frac{\partial}{\partial U_2}\left\{\frac{a_2}{\mathscr{D}_2}\left[\left(-b_2\frac{\partial \zeta_2}{\partial b_2} - c_2\frac{\partial \zeta_2}{\partial c_2}\right)(E - E_v) + \frac{\partial \zeta_2}{\partial b_2}(F - F_v) + \frac{\partial \zeta_2}{\partial c_2}(G - G_v)\right]\right\} \tag{C2}$$

Clearly, these Jacobians have an inviscid part and a viscous part:

$$\frac{\partial F_2}{\partial U_2} = \left(\frac{\partial F_2}{\partial U_2}\right)_{\text{inviscid}} - \left(\frac{\partial F_2}{\partial U_2}\right)_{\text{viscous}} \tag{C3}$$

$$\frac{\partial G_2}{\partial U_2} = \left(\frac{\partial G_2}{\partial U_2}\right)_{\text{inviscid}} - \left(\frac{\partial G_2}{\partial U_2}\right)_{\text{viscous}} \tag{C4}$$

The inviscid part can be written as a linear combination of $\partial E/\partial U$, $\partial F/\partial U$, $\partial G/\partial U$

$$\left(\frac{\partial F_2}{\partial U_2}\right)_{\text{inviscid}} = \frac{1}{a_2}\left(a_2\frac{\partial \eta_2}{\partial a_2} - b_2\frac{\partial \eta_2}{\partial b_2} - c_2\frac{\partial \eta_2}{\partial c_2}\right)\frac{\partial E}{\partial U} + \frac{1}{a_2}\frac{\partial \eta_2}{\partial b_2}\frac{\partial F}{\partial U} + \frac{1}{a_2}\frac{\partial \eta_2}{\partial c_2}\frac{\partial G}{\partial U} \tag{C5}$$

$$\left(\frac{\partial G_2}{\partial U_2}\right)_{\text{inviscid}} = \frac{1}{a_2}\left(-b_2\frac{\partial \zeta_2}{\partial b_2} - c_2\frac{\partial \zeta_2}{\partial c_2}\right)\frac{\partial E}{\partial U} + \frac{1}{a_2}\frac{\partial \zeta_2}{\partial b_2}\frac{\partial F}{\partial U} + \frac{1}{a_2}\frac{\partial \zeta_2}{\partial c_2}\frac{\partial G}{\partial U} \tag{C6}$$

where

$$\frac{\partial E}{\partial U} = \begin{bmatrix} 0 & 1 & 0 & 0 & 0 \\ \frac{\gamma-3}{2}u^2 + \frac{\gamma-1}{2}(v^2+w^2) & (3-\gamma)u & -(\gamma-1)v & -(\gamma-1)w & \gamma-1 \\ -uv & v & u & 0 & 0 \\ -uw & w & 0 & u & 0 \\ [-\gamma e_t + (\gamma-1)(u^2+v^2+w^2)]u & \gamma e_t - (\gamma-1)\frac{3u^2+v^2+w^2}{2} & -(\gamma-1)uv & -(\gamma-1)uw & \gamma u \end{bmatrix} \tag{C7}$$

$$\frac{\partial F}{\partial U} = \begin{bmatrix} 0 & 0 & 1 & 0 & 0 \\ -uv & v & u & 0 & 0 \\ \frac{\gamma-1}{2}(u^2+w^2)+\frac{\gamma-3}{2}v^2 & -(\gamma-1)u & (3-\gamma)v & -(\gamma-1)w & \gamma-1 \\ -vw & 0 & w & v & 0 \\ [-\gamma e_t+(\gamma-1)(u^2+v^2+w^2)]v & -(\gamma-1)uv & \gamma e_t-\frac{\gamma-1}{2}(u^2+3v^2+w^2) & -(\gamma-1)vw & \gamma v \end{bmatrix} \tag{C8}$$

$$\frac{\partial G}{\partial U} = \begin{bmatrix} 0 & 0 & 0 & 1 & 0 \\ -uw & w & 0 & u & 0 \\ -vw & 0 & w & v & 0 \\ \frac{\gamma-1}{2}(u^2+v^2)+\frac{\gamma-3}{2}w^2 & -(\gamma-1)u & -(\gamma-1)v & (3-\gamma)w & \gamma-1 \\ [-\gamma e_t+(\gamma-1)(u^2+v^2+w^2)]w & -(\gamma-1)uw & -(\gamma-1)vw & \gamma e_t-\frac{\gamma-1}{2}(u^2+v^2+3w^2) & \gamma w \end{bmatrix} \tag{C9}$$

The viscous part of the Jacobians is

$$\left(\frac{\partial F_2}{\partial U_2}\right)_{\text{viscous}} = \frac{\partial}{\partial U_2}\left\{\frac{a_2}{\mathscr{D}_2}\left[\left(a_2\frac{\partial \eta_2}{\partial a_2}-b_2\frac{\partial \eta_2}{\partial b_2}-c_2\frac{\partial \eta_2}{\partial c_2}\right)E_v+\frac{\partial \eta_2}{\partial b_2}F_v+\frac{\partial \eta_2}{\partial c_2}G_v\right]\right\} \tag{C10}$$

$$\left(\frac{\partial F_2}{\partial U_2}\right)_{\text{viscous}} = \frac{\mu}{\mathscr{D}_2 \mathrm{Re}_L}$$

$$\begin{bmatrix}
0 & 0 & 0 & 0 & 0 \\
-\left[\ell_1\left(\frac{\mathscr{D}_2}{a_2^2}\frac{u}{\rho}\right)_{\eta_2} + \ell_4\left(\frac{\mathscr{D}_2}{a_2^2}\frac{v}{\rho}\right)_{\eta_2} + \ell_5\left(\frac{\mathscr{D}_2}{a_2^2}\right)\frac{w}{\rho}_{\eta_2}\right] & \ell_1\left(\frac{\mathscr{D}_2}{a_2^2}\frac{1}{\rho}\right)_{\eta_2} & \ell_4\left(\frac{\mathscr{D}_2}{a_2^2}\frac{1}{\rho}\right)_{\eta_2} & \ell_5\left(\frac{\mathscr{D}_2}{a_2^2}\frac{1}{\rho}\right)_{\eta_2} & 0 \\
-\left[\ell_4\left(\frac{\mathscr{D}_2}{a_2^2}\frac{u}{\rho}\right)_{\eta_2} + \ell_2\left(\frac{\mathscr{D}_2}{a_2^2}\frac{v}{\rho}\right)_{\eta_2} + \ell_6\left(\frac{\mathscr{D}_2}{a_2^2}\frac{w}{\rho}\right)_{\eta_2}\right] & \ell_4\left(\frac{\mathscr{D}_2}{a_2^2}\frac{1}{\rho}\right)_{\eta_2} & \ell_2\left(\frac{\mathscr{D}_2}{a_2^2}\frac{1}{\rho}\right)_{\eta_2} & \ell_6\left(\frac{\mathscr{D}_2}{a_2^2}\frac{1}{\rho}\right)_{\eta_2} & 0 \\
-\left[\ell_5\left(\frac{\mathscr{D}_2}{a_2^2}\frac{u}{\rho}\right)_{\eta_2} + \ell_6\frac{\mathscr{D}_2}{a_2^2}\frac{v}{\rho}_{\eta_2} + \ell_3\left(\frac{\mathscr{D}_2}{a_2^2}\frac{w}{\rho}\right)_{\eta_2}\right] & \ell_5\left(\frac{\mathscr{D}_2}{a_2^2}\frac{1}{\rho}\right)_{\eta_2} & \ell_6\left(\frac{\mathscr{D}_2}{a_2^2}\frac{1}{\rho}\right)_{\eta_2} & \ell_3\left(\frac{\mathscr{D}_2}{a_2^2}\frac{1}{\rho}\right)_{\eta_2} & 0 \\
\begin{array}{l} -\ell_1\left(\frac{\mathscr{D}_2}{a_2^2}\frac{u^2}{\rho}\right)_{\eta_2} - \ell_2\left(\frac{\mathscr{D}_2}{a_2^2}\frac{v^2}{\rho}\right)_{\eta_2} \\ -\ell_3\left(\frac{\mathscr{D}_2}{a_2^2}\frac{w^2}{\rho}\right)_{\eta_2} - 2\ell_4\left(\frac{\mathscr{D}_2}{a_2^2}\frac{uv}{\rho}\right)_{\eta_2} \\ -2\ell_5\left(\frac{\mathscr{D}_2}{a_2^2}\frac{uw}{\rho}\right)_{\eta_2} - 2\ell_6\left(\frac{\mathscr{D}_2}{a_2^2}\frac{vw}{\rho}\right)_{\eta_2} \\ -\ell_7\left\{\frac{\mathscr{D}_2}{a_2^2}\left[\frac{p}{(\gamma-1)\rho^2} - \frac{u^2+v^2+w^2}{2}\right]\right\}_{\eta_2} \end{array} & \begin{array}{l} \ell_1\left(\frac{\mathscr{D}_2}{a_2^2}\frac{u}{\rho}\right)_{\eta_2} \\ +\ell_4\left(\frac{\mathscr{D}_2}{a_2^2}\frac{v}{\rho}\right)_{\eta_2} \\ +\ell_6\left(\frac{\mathscr{D}_2}{a_2^2}\frac{w}{\rho}\right)_{\eta_2} \\ -\ell_7\left(\frac{\mathscr{D}_2}{a_2^2}\frac{u}{\rho}\right)_{\eta_2} \end{array} & \begin{array}{l} \ell_4\left(\frac{\mathscr{D}_2}{a_2^2}\frac{u}{\rho}\right)_{\eta_2} \\ +\ell_2\left(\frac{\mathscr{D}_2}{a_2^2}\frac{v}{\rho}\right)_{\eta_2} \\ +\ell_6\left(\frac{\mathscr{D}_2}{a_2^2}\frac{w}{\rho}\right)_{\eta_2} \\ -\ell_7\left(\frac{\mathscr{D}_2}{a_2^2}\frac{v}{\rho}\right)_{\eta_2} \end{array} & \begin{array}{l} \ell_5\left(\frac{\mathscr{D}_2}{a_2^2}\frac{u}{\rho}\right)_{\eta_2} \\ +\ell_6\left(\frac{\mathscr{D}_2}{a_2^2}\frac{v}{\rho}\right)_{\eta_2} \\ +\ell_3\left(\frac{\mathscr{D}_2}{a_2^2}\frac{w}{\rho}\right)_{\eta_2} \\ -\ell_7\left(\frac{\mathscr{D}_2}{a_2^2}\frac{w}{\rho}\right)_{\eta_2} \end{array} & \ell_7\left(\frac{\mathscr{D}_2}{a_2^2}\frac{1}{\rho}\right)_{\eta_2}
\end{bmatrix} \tag{C11}$$

where

$$\left.\begin{aligned}
\ell_1 &= \frac{4}{3}\bar{\ell}_1^2 + \bar{\ell}_2^2 + \bar{\ell}_3^2 & \ell_5 &= \frac{\bar{\ell}_1\bar{\ell}_3}{3} \\
\ell_2 &= \bar{\ell}_1^2 + \frac{4}{3}\bar{\ell}_2^2 + \bar{\ell}_3^2 & \ell_6 &= \frac{\bar{\ell}_2\bar{\ell}_3}{3} \\
\ell_3 &= \bar{\ell}_1^2 + \bar{\ell}_2^2 + \frac{4}{3}\bar{\ell}_3^2 & \ell_7 &= \frac{\gamma}{\mathrm{Pr}}\left(\bar{\ell}_1^2 + \bar{\ell}_2^2 + \bar{\ell}_3^2\right) \\
\ell_4 &= \frac{\bar{\ell}_1\bar{\ell}_2}{3}
\end{aligned}\right\} \tag{C12}$$

$$\left.\begin{aligned} \bar{\ell}_1 &= a_2 \frac{\partial \eta_2}{\partial a_2} - b_2 \frac{\partial \eta_2}{\partial b_2} - c_2 \frac{\partial \eta_2}{\partial c_2} \qquad \bar{\ell}_3 = \frac{\partial \eta_2}{\partial c_2} \\ \bar{\ell}_2 &= \frac{\partial \eta_2}{\partial b_2} \end{aligned}\right\} \tag{C13}$$

and $(\cdot)_{\eta_2}$ indicates derivative with respect to η_2. Similarly

$$\left(\frac{\partial G_2}{\partial U_2}\right)_{\text{viscous}} = \frac{\partial}{\partial U_2}\left\{\frac{a_2}{\mathscr{D}_2}\left[\left(-b_2 \frac{\partial \zeta_2}{\partial b_2} - c_2 \frac{\partial \zeta_2}{\partial c_2}\right)E_v + \frac{\partial \zeta_2}{\partial b_2} F_v + \frac{\partial \zeta_2}{\partial c_2} G_v\right]\right\} \tag{C14}$$

$$\left(\frac{\partial G_2}{\partial U_2}\right)_{\text{viscous}} = \frac{\mu}{\mathscr{D}_2 \mathrm{Re}_L}$$

$$\begin{bmatrix}
0 & 0 & 0 & 0 & 0 \\
-\left[m_1\left(\frac{\mathscr{D}_2}{a_2^2}\frac{u}{\rho}\right)_{\zeta_2} + m_4\left(\frac{\mathscr{D}_2}{a_2^2}\frac{v}{\rho}\right)_{\zeta_2} + m_5\left(\frac{\mathscr{D}_2}{a_2^2}\frac{w}{\rho}\right)_{\zeta_2}\right] & m_1\left(\frac{\mathscr{D}_2}{a_2^2}\frac{1}{\rho}\right)_{\zeta_2} & m_4\left(\frac{\mathscr{D}_2}{a_2^2}\frac{1}{\rho}\right)_{\zeta_2} & m_5\left(\frac{\mathscr{D}_2}{a_2^2}\frac{1}{\rho}\right)_{\zeta_2} & 0 \\
-\left[m_4\left(\frac{\mathscr{D}_2}{a_2^2}\frac{u}{\rho}\right)_{\zeta_2} + m_2\left(\frac{\mathscr{D}_2}{a_2^2}\frac{v}{\rho}\right)_{\zeta_2} + m_6\left(\frac{\mathscr{D}_2}{a_2^2}\frac{w}{\rho}\right)_{\zeta_2}\right] & m_4\left(\frac{\mathscr{D}_2}{a_2^2}\frac{1}{\rho}\right)_{\zeta_2} & m_2\left(\frac{\mathscr{D}_2}{a_2^2}\frac{1}{\rho}\right)_{\zeta_2} & m_6\left(\frac{\mathscr{D}_2}{a_2^2}\frac{1}{\rho}\right)_{\zeta_2} & 0 \\
-\left[m_5\left(\frac{\mathscr{D}_2}{a_2^2}\frac{u}{\rho}\right)_{\zeta_2} + m_6\left(\frac{\mathscr{D}_2}{a_2^2}\frac{v}{\rho}\right)_{\zeta_2} + m_3\left(\frac{\mathscr{D}_2}{a_2^2}\frac{w}{\rho}\right)_{\zeta_2}\right] & m_5\left(\frac{\mathscr{D}}{a_2^2}\frac{1}{\rho}\right)_{\zeta_2} & m_6\left(\frac{\mathscr{D}_2}{a_2^2}\frac{1}{\rho}\right)_{\zeta_2} & m_3\left(\frac{\mathscr{D}_2}{a_2^2}\frac{1}{\rho}\right)_{\zeta_2} & 0 \\
\begin{aligned} &- m_1\left(\frac{\mathscr{D}_2}{a_2^2}\frac{u^2}{\rho}\right)_{\zeta_2} - m_2\left(\frac{\mathscr{D}_2}{a_2^2}\frac{v^2}{\rho}\right)_{\zeta_2} \\ &- m_3\left(\frac{\mathscr{D}_2}{a_2^2}\frac{w^2}{\rho}\right)_{\zeta_2} - 2m_4\left(\frac{\mathscr{D}_2}{a_2^2}\frac{uv}{\rho}\right)_{\zeta_2} \\ &- 2m_5\left(\frac{\mathscr{D}_2}{a_2^2}\frac{uw}{\rho}\right)_{\zeta_2} - 2m_6\left(\frac{\mathscr{D}_2}{a_2^2}\frac{vw}{\rho}\right)_{\zeta_2} \\ &- m_7\left\{\frac{\mathscr{D}_2}{a_2^2}\left[\frac{p}{(\gamma-1)\rho^2} - \frac{u^2+v^2+w^2}{2\rho}\right]\right\}_{\zeta_2} \end{aligned} & \begin{aligned} &m_1\left(\frac{\mathscr{D}_2}{a_2^2}\frac{u}{\rho}\right)_{\zeta_2} \\ &+ m_4\left(\frac{\mathscr{D}_2}{a_2^2}\frac{v}{\rho}\right)_{\zeta_2} \\ &+ m_5\left(\frac{\mathscr{D}_2}{a_2^2}\frac{w}{\rho}\right)_{\zeta_2} \\ &- m_7\left(\frac{\mathscr{D}_2}{a_2^2}\frac{u}{\rho}\right)_{\zeta_2} \end{aligned} & \begin{aligned} &m_4\left(\frac{\mathscr{D}_2}{a_2^2}\frac{u}{\rho}\right)_{\zeta_2} \\ &+ m_2\left(\frac{\mathscr{D}_2}{a_2^2}\frac{v}{\rho}\right)_{\zeta_2} \\ &+ m_6\left(\frac{\mathscr{D}_2}{a_2^2}\frac{w}{\rho}\right)_{\zeta_2} \\ &- m_7\left(\frac{\mathscr{D}_2}{a_2^2}\frac{v}{\rho}\right)_{\zeta_2} \end{aligned} & \begin{aligned} &m_5\left(\frac{\mathscr{D}_2}{a_2^2}\frac{u}{\rho}\right)_{\zeta_2} \\ &+ m_6\left(\frac{\mathscr{D}_2}{a_2^2}\frac{v}{\rho}\right)_{\zeta_2} \\ &+ m_3\left(\frac{\mathscr{D}_2}{a_2^2}\frac{w}{\rho}\right)_{\zeta_2} \\ &- m_7\left(\frac{\mathscr{D}_2}{a_2^2}\frac{w}{\rho}\right)_{\zeta_2} \end{aligned} & m_7\left(\frac{\mathscr{D}_2}{a_2^2}\frac{1}{\rho}\right)_{\zeta_2}
\end{bmatrix} \tag{C15}$$

where:

$$
\left.
\begin{aligned}
m_1 &= \frac{4}{3}\bar{m}_1^2 + \bar{m}_2^2 + \bar{m}_3^2 & m_5 &= \frac{\bar{m}_1\bar{m}_3}{3} \\
m_2 &= \bar{m}_1^2 + \frac{4}{3}\bar{m}_2^2 + \bar{m}_3^2 & m_6 &= \frac{\bar{m}_2\bar{m}_3}{3} \\
m_3 &= \bar{m}_1^2 + \bar{m}_2^2 + \frac{4}{3}\bar{m}_3^2 & m_7 &= \frac{\gamma}{Pr}\left(\bar{m}_1^2 + \bar{m}_2^2 + \bar{m}_3^2\right) \\
m_4 &= \frac{\bar{m}_1\bar{m}_2}{3}
\end{aligned}
\right\} \quad (C16)
$$

$$
\left.
\begin{aligned}
\bar{m}_1 &= -b_2\frac{\partial\zeta_2}{\partial b_2} - c_2\frac{\partial\zeta_2}{\partial c_2} & \bar{m}_2 &= \frac{\partial\zeta_2}{\partial c_2} \\
\bar{m}_2 &= \frac{\partial\zeta_2}{\partial b_2}
\end{aligned}
\right\} \quad (C17)
$$

and $(\cdot)_{\zeta_2}$ indicates derivatives with respect to ζ_2. In these viscous Jacobians, the cross derivative viscous terms have been neglected and the coefficient of molecular viscosity has been assumed to depend only on the position, not on the vector U.

Finally, the Jacobian $\partial E_2^*/\partial U_2$ is given by

$$
\frac{\partial E_2^*}{\partial U_2} = \begin{bmatrix}
0 & 1 & 0 & 0 & 0 \\
\frac{\omega(\gamma-1)-2}{2}u^2 + \frac{\omega(\gamma-1)}{2}(v^2+w^2) & [2-\omega(\gamma-1)]u & -\omega(\gamma-1)v & -\omega(\gamma-1)v & \omega(\gamma-1) \\
-uv & v & u & 0 & 0 \\
-uw & w & 0 & u & 0 \\
[-\gamma e_t + (\gamma-1)(u^2+v^2+w^2)]u & \gamma e_t - (\gamma-1)\frac{3u^2+v^2+w^2}{2} & -(\gamma-1)uv & -(\gamma-1)uw & \gamma u
\end{bmatrix}
\quad (C18)
$$